ESTUDIO DEL DESEMPEÑO DE TURBINAS DARRIEUS CONTRARROTATORIAS EN PROXIMIDAD

TESIS

QUE PARA OBTENER EL TÍTULO DE:

Doctor en Ingeniería Mecánica

PRESENTA:

Edgar Alejandro Martínez Ojeda

DIRECTOR DEL TRABAJO:
Dr. Francisco Javier Solorio Ordaz

Ciudad Universitaria, 01/12/2021

Contents

List of Figures

List of Tables

Chapter 1

Abstract

The actuator-cylinder model was implemented in OpenFOAM by virtue of source terms in the Navier–Stokes equations. Since the stand-alone actuator cylinder is not able to properly model the wake of a vertical-axis wind turbine, the steady incompressible flow solver simpleFoam provided by OpenFOAM was used to resolve the entire flow and wakes of the turbines. The source terms are only applied inside a certain region of the computational domain, namely a finite-thickness cylinder which represents the flight path of the blades. One of the major advantages of this approach is its implicitness – that is, the velocities inside the hollow cylinder region feed the stand-alone actuator-cylinder model (AC); this in turn computes the volumetric forces and passes them to the OpenFOAM solver in order to be applied inside the hollow cylinder region. The process is repeated in each iteration of the solver until convergence is achieved. The model was compared against experimental works; wake deficits and power coefficients are used in order to assess the validity of the model. Overall, there is a good agreement of the pattern of the power coefficients according to the positions of the turbines in the array. The actual accuracy of the power coefficient depends strongly on the solidity of the turbine (actuator cylinder related) and both the inlet boundary turbulence intensity and turbulence length scale (RANS simulation related).

Last, the virtual AC was used to study the performance of two different arrays of wind turbines. A staggered array proved to be more efficient than a fish-school array in most directions; however, the fish-school array outperformed the conventional staggered array when the pairs of turbines were facing the wind. Increases in global power coefficient up to 16% were found when the wind speed was 8 m s^{-1} and up to 10% when the wind speed was 10 m s^{-1} . Despite the fish-school array being slightly less efficient, this array yielded almost twice as much power density as the staggered array in almost all directions.

Chapter 2

Resumen

Se implementó un cilindro virtual en OpenFOAM mediante los términos fuente en las ecuaciones de Navier-Stokes. Debido a que el cilindro virtual no es capaz de modelar la estela de la turbina por sí solo, el solucionador para flujo turbulento e incompresible simpleFoam fue usado para resolver el campo de velocidades del dominio. Los términos fuente solamente se aplican en una región que forma un cilindro hueco, donde pasan las aspas de la turbina. Las fuerzas volumétricas son calculadas por el cilindro virtual y posteriormente aplicadas en la región correspondiente, esto desacelera el fluido y se crea una estela similar a la de una turbina. El modelo se verificó y validó con trabajos experimentales y teóricos. Hubo buena concordancia en cuanto al patrón de los coeficientes de potencia de cada turbina respecto a su posición. La precisión del modelo depende de la solidez de la turbina y de las condiciones de frontera impuestas en el dominio computacional.

Por último, se utilizó el modelo para comparar el desempeño de dos tipos de arreglos de granjas de turbinas. La granja escalonada resultó ser más eficiente que la granja de pares en la mayoría de las direcciones de incidencia del viento. Sin embargo; la granja de pares superó a la granja convencional escalonada en cuanto a densidad de potencia, especialmente cuando el par de turbinas miraba hacia al viento. El promedio de la densidad de potencia de todas las direcciones del viento para la granja de pares fue casi del doble, dependiendo de la velocidad del viento. Se cree que con una posición estratégica de las turbinas se puede compactar la granja en un terreno dos veces menor y aún así conseguir casi el doble de energía durante todo el año.

Chapter 3

Introduction

Vertical-axis wind turbines have been experiencing a surge during the last decades, mainly due to the availability of new materials as well as machinery that is especially designed for vertical-axis wind turbines (VAWT). Initially, these turbines were meant to be used in large-scale wind farms but unfortunately the turbines could not withstand the wind loads as well as fatigue from vibration problems [2]. Once the eighties were over these projects were largely abandoned and interest in VAWTs was lost. Recently, researchers, builders and even amateurs have tried success using VAWTs in residential applications but the efforts have been thwarted by the superiority of horizontal-axis wind turbines (HAWT) which are able to reach much higher revolutions per minute and higher efficiencies. Many small manufacturers have gone bankrupt or have been unable to catch up with HAWT markets.

Nowadays offshore wind power has been taking over and companies such as SeaTwirl are beginning to build vertical-axis wind turbines designed for offshore applications [3]. Claims from academia even go as far as to say that placing these turbines close to each other –forming pairs– can cause an increase up to 15% in power [4]. This can reducing land area costs while increasing the power density of the farm.

Installing VAWTs next to roads is also a recent concept that is meant to charge batteries that will light the roads. This idea employs Savonius turbines, to be precise. Savonius turbines usually employ blades that resemble a bucket which has been cut in half, these turbines are able to self-start at lower revolutions per minute. The energy will come from the wakes of cars and trucks.

Some of the models employed to study VAWTs are the multiple stream-tube model, the double multiple stream-tube model [5], the actuator cylinder [6], vortex lattice models and vortex panel model, etc. The double multiple stream-tube model is based on the momentum theory and the blade element method. The turbine is seen as a series of multiple stream-tubes with actuators on the upstream and downstream parts of the rotor, it is able to compute the forces acting on the blade as well as the whole power coefficient of the turbine. The actuator cylinder on the other hand, is a solution of the Euler equations, the source terms in the Euler equations are treated as volumetric forces exerted by the turbine, this elegant solution can resolve the entire velocity field if the force distribution along the flight path is known. In order to close the system of equations, the blade element theory is needed and an iterative solution is achieved.

While these last two methods described above are useful for the analysis of a single turbine, they are hard to implement on multiple turbines. The author of this work generalized the actuator cylinder model for multiple turbines but the fading of the wakes was unrealistic due to the inviscid nature of the solution –the wakes do not vanish. Therefore a search for a model that could analyze wind farms and predict their wakes was undertaken.

The modeling of vertical-axis wind turbine farms has also lacked researched in the last years compared to horizontal-axis wind turbines. The complexity of the models ranges from simple momentum models to full-rotor Reynolds-averaged Navier-Stokes equations or large-eddy simulations. While simple models are computationally inexpensive, they lack accuracy and rely on various semi-empirical corrections which may not be valid for all cases; high-fidelity simulations are simply out of the scope of many researchers and scientists due to the tremendous computational requirements.

The models that have been used for wind farm modeling will be listed according to complexity, their benefits and caveats will be listed below.

The first category belongs to models using the momentum theory or potential flow theory. One of the simplest wake model is the Jensen model [7], which is able to describe the wake shape provided the thrust coefficient and induction factors are given. The rate of growth of the wake depends on empirical constants. The model can be extended to multiple turbines using a superposition technique. Although it was originally developed for HAWTs, some researchers have developed similar models for VAWTs [8] achieving good results for the wake shape. Potential flow models try to emulate the wake of a turbine by superposing many different potential flows such as a uniform stream, a dipole and a vortex [9]. The wake deficit can be modeled as a probabilistic density function and it is simply subtracted from the flow field. This model has also been extended to multiple-turbine environments [10] but it is still very problem-dependent and needs much more calibration since it is unable to model viscous effects.

The next category belongs to actuator models. These models rely on replacing the turbine's blades by volumetric forces. [11] has successfully implemented a RANS actuator disc model for a HAWT in OpenFOAM. The model is explicit and it requires the values of thrust and torque; although it can be extended to multiple turbines, it relies on the assumption of all turbines having the same thrust and torque, which may not be entirely true for turbines in the back rows. [12] has also developed actuator line models for both HAWTs and VAWTs with the option of using either RANS or LES. [1, 13, 14] have also performed LES simulations of actuator line models on a single VAWT. An interesting multi-turbine simulation using an actuator line model was done by [15], the study works on the effect of clustering the turbines in order to increase the power density.

The last category of models employs full-rotor RANS simulations. Works on multiple VAWTs can be found in [16, 17, 18]. Recently, a very interesting study by [4] was done on pairs and triplets of VAWTs, the study claims that a 15% increase in power can be achieved if turbines are placed closer. Although these claims are done on the basis of 2D simulations, it is not sure whether this effect may scale up to a wind farm.

Therefore, the purpose of this thesis is to come up with a new model that is computationally cheap and able to resolve the wakes of turbine. The actuator cylinder model was chosen as a surrogate model which will compute the volumetric forces of the turbine and pass them to an OpenFOAM RANS solver as source terms in the momentum equations; the forces will block the flow, thereby creating a wake. The OpenFOAM simpleFoam solver (incompressible and turbulent flows) will then resolve the entire pressure and velocity field.

The thesis is organized in the following way: a chapter devoted to the original actuator cylinder model as well as some verifications; a chapter dedicated to the RANS solver using the actuator cylinder as the surrogate model; and a last chapter dedicated to a case study of different types of wind farm arrays.

Chapter 4

The Actuator Cylinder Model

This chapter will explain the actuator cylinder model. Many other relatively simple models are available, they are mostly based on the momentum theory and the blade element theory. The current model is chosen because it can be generalized to many turbines (although the wake effects cannot be captured realistically). Moreover it will be used in the subsequent chapter as it will be incorporated into a CFD code in order to create a virtual turbine, that is, volumetric forces will replace the effects of the actual blades.

The vertical-axis wind turbine can be modeled as a cylindrical surface upon which radial volume forces act, this will, in turn, create a pressure jump Δp across the entire surface. The turbine's blades are responsible for these radial forces. Madsen [6] devised this model in the early eighties, he states that the normal loads are a result of the volume forces integrated along the thickness of the actuator cylinder as shown in the next equation (Δp has been replaced by Q_n in order to denote normal forces per unit length averaged over one revolution).

$$Q_n(\theta) = \lim_{\epsilon \to 0} \int_{R-\epsilon}^{R+\epsilon} f_n(\theta) \cdot dr \tag{4.1}$$

Figure 4.1 depicts an upper view of an infinite long actuator cylinder (in the z-direction). Q_n represents the normal load at angular position θ, $f_n(\theta)$ is the volumetric force and the incoming wind velocity is represented by V_∞. Notice that θ is zero at the conventional $\theta = 90°$. The governing equations are the equation of continuity and the steady-state Euler equations. Velocities in the x and y directions are to be non-dimensionalized by the incoming wind velocity V_∞; lengths are non-dimensionalized by the wind turbine radius R and pressure is non-dimensionalized by ρV_∞^2.
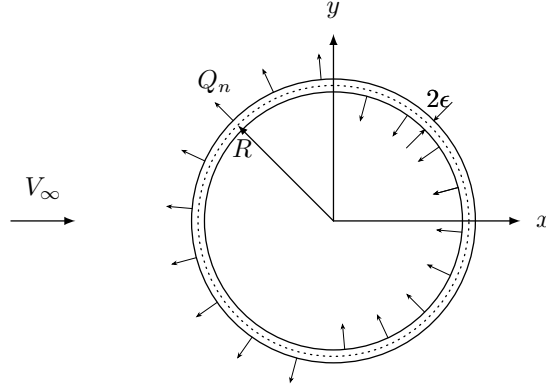
Figure 4.1: *The radial forces acting upon the actuator cylinder's surface.*

The non-dimensional velocities in the Euler's equations are expressed as functions of the perturbation velocities:

$$v_x = 1 + w_x \tag{4.2}$$

$$v_y = w_y \tag{4.3}$$

The reason being, is that the velocities on the very surface of the cylinder will not be the same as those in the free stream due to lost of momentum. The non-dimensional volume force components in x and y are represented by f_x and f_y respectively. The non-dimensional Euler's equation then become:

$$\frac{\partial w_x}{\partial x} + w_x \frac{\partial w_x}{\partial x} + w_y \frac{\partial w_x}{\partial y} = -\frac{\partial p}{\partial x} + f_x \tag{4.4}$$

$$\frac{\partial w_y}{\partial x} + w_x \frac{\partial w_y}{\partial x} + w_y \frac{\partial w_y}{\partial y} = -\frac{\partial p}{\partial y} + f_y \tag{4.5}$$

The equation of continuity:

$$\frac{\partial w_x}{\partial x} + \frac{\partial w_y}{\partial y} = 0 \tag{4.6}$$

The non-linear terms in equations 4.4 and 4.5 are grouped into g_x and g_y, which can be seen as second-order volume forces.

$$\frac{\partial w_x}{\partial x} = -\frac{\partial p}{\partial x} + f_x + g_x \tag{4.7}$$

$$\frac{\partial w_y}{\partial x} = -\frac{\partial p}{\partial y} + f_y + g_y \tag{4.8}$$

Differentiating 4.7 with respect to x and 4.8 with respect to y yields to:

$$\frac{\partial^2 w_x}{\partial x^2} = -\frac{\partial^2 p}{\partial x^2} + \frac{\partial f_x}{\partial x} + \frac{\partial g_x}{\partial x} \tag{4.9}$$

$$\frac{\partial^2 w_y}{\partial x \partial y} = -\frac{\partial^2 p}{\partial y^2} + \frac{\partial f_y}{\partial y} + \frac{\partial g_y}{\partial y} \tag{4.10}$$

The continuity equation is also differentiated with respect to x:

$$\frac{\partial^2 w_x}{\partial x^2} + \frac{\partial^2 w_y}{\partial x \partial y} = 0 \tag{4.11}$$

Finally, summing both equation 4.9 and equation 4.10 yields to a Poisson type equation for the pressure.

$$\frac{\partial^2 p}{\partial x^2} + \frac{\partial^2 p}{\partial y^2} = \left(\frac{\partial f_x}{\partial x} + \frac{\partial f_y}{\partial y} \right) + \left(\frac{\partial g_x}{\partial x} + \frac{\partial g_y}{\partial y} \right) \tag{4.12}$$

Given that the pressure equals zero far away from the actuator cylinder, the solution can be broken down into a linear part and a nonlinear part.

$$p(f) = \frac{1}{2\pi} \int \int \frac{f_x(x - \xi) + f_y(y - \eta)}{(x - \xi)^2 + (y - \eta)^2} d\xi d\eta \tag{4.13}$$

$$p(g) = \frac{1}{2\pi} \int \int \frac{g_x(x - \xi) + g_y(y - \eta)}{(x - \xi)^2 + (y - \eta)^2} d\xi d\eta \tag{4.14}$$

These integrals must be performed throughout the surface of the actuator cylinder since this is precisely the blade's flight path. Equations 4.7 and 4.8 are integrated with respect to x yielding:

$$w_x = -p(f) + \int_{-\infty}^{x} f_x \cdot dx' - p(g) + \int_{-\infty}^{x} g_x \cdot dx' \tag{4.15}$$

$$w_y = -\int_{-\infty}^{x} \frac{\partial}{\partial y} p(f) dx' + \int_{-\infty}^{x} f_y \cdot dx' - \int_{-\infty}^{x} \frac{\partial}{\partial y} p(g) dx' + \int_{-\infty}^{x} g_y \cdot dx' \tag{4.16}$$

The terms containing g in the last two equations belong to the non-linear solution, these terms will be neglected for the time being. In subsequent sections, a modification of the linear solution will be shown to make up for the non-linear part of the solution. Meanwhile, equation 4.13 needs to be expressed in terms of polar coordinates, since ξ and η are the dummy variables in the x and y directions respectively. Note that the non-dimensional radius of the turbine equals one, while the azimuth angle θ takes the value of zero at $y = 1$. Therefore, equation 4.13 becomes.

$$p(f) = \frac{1}{2\pi} \int_0^{2\pi} \Delta p(\theta) \frac{-(x + \sin(\theta)) \sin(\theta) + (y - \cos(\theta)) \cos(\theta)}{(x + \sin(\theta))^2 + (y - \cos(\theta))^2} d\theta \tag{4.17}$$

After working out the integrals in equations 4.15 and 4.16, the perturbation velocities are shown to be:

$$\begin{aligned} w_x = &-\frac{1}{2\pi} \int_0^{2\pi} \Delta p(\theta) \frac{-(x + \sin(\theta)) \sin(\theta) + (y - \cos(\theta)) \cos(\theta)}{(x + \sin(\theta))^2 + (y - \cos(\theta))^2} d\theta \\ &- \Delta p(\arccos(y))^* + \Delta p(-\arccos(y))^{**} \end{aligned} \tag{4.18}$$

$$w_y = -\frac{1}{2\pi} \int_0^{2\pi} \Delta p(\theta) \frac{-(x + \sin(\theta)) \cos(\theta) - (y - \cos(\theta)) \sin(\theta)}{(x + \sin(\theta))^2 + (y - \cos(\theta))^2} d\theta \tag{4.19}$$

When the evaluation takes place inside the cylinder, the $*$ term must be included; on the other hand, if the evaluation point is located in the wake (the leeward part of the cylinder), both the $*$ and the $**$ terms must be included in the equation. The Δp term can be replaced by Q_n, thus this will be the nomenclature for the normal loads. The previous derivation is contained in Appendix A.

4.1   Numerical Solution

The typical approach is to divide the cylinder's surface into a finite number of evaluation points, that is, the perturbation velocities along the flight path of the blades will be determined. The step between two points is then:

$$\Delta\theta = 2\pi/N \tag{4.20}$$

Where N is the total number of evaluation points. It is assumed that the normal loads are piecewise constant, this means that the property to be evaluated is constant throughout each sector.

Equations 4.18 and 4.19 can be re-written as:

$$w_x = -\frac{1}{2\pi}\sum_{i=0}^{N-1}Q_{n,i}\int_{\theta_i-\frac{1}{2}\Delta\theta}^{\theta_i+\frac{1}{2}\Delta\theta}\frac{-(x+\sin(\phi))\sin(\phi)+(y-\cos(\phi))\cos(\phi)}{(x+\sin(\phi))^2+(y-\cos(\phi))^2}d\phi \tag{4.21}$$
$$- Q_n(\arccos(y))^* + Q_n(-\arccos(y))^{**}$$

$$w_y = -\frac{1}{2\pi}\sum_{i=0}^{N-1}Q_{n,i}\int_{\theta_i-\frac{1}{2}\Delta\theta}^{\theta_i+\frac{1}{2}\Delta\theta}\frac{-(x+\sin(\phi))\cos(\phi)-(y-\cos(\phi))\sin(\phi)}{(x+\sin(\phi))^2+(y-\cos(\phi))^2}d\phi \tag{4.22}$$

It is important to note that x and y refer to the coordinates of the point on which the perturbation velocities are to be determined, while the subscript i refers to the *i-eth* of the total N points the flight path was divided into, namely, evaluation points; θ refers to the azimuthal location of the evaluation points, while ϕ is just a dummy variable used to integrate along each sector. It's also important to realize that since the normal loadings are assumed to be piecewise constant, they can be taken out of each of the N integrals.

According to Madsen[6], problems due to certain singularities –division by zero– could arise in equations 4.21 and 4.22. He recommends to offset the control points (on which the perturbation velocities are wished to be known, namely j) ever so slightly outside the cylinder. Thus, the offset factor for both x and y lies between 0.1% and 1%. The offsetted control points are given by the following expressions:

$$x_j = -f\sin\theta \tag{4.23}$$

$$y_j = f\cos\theta \tag{4.24}$$

The j and i nomenclature is according to Li[19]. However, offsetting the control points will make all of them lie just outside the cylinder, this means that the $*$ and $**$ terms will only be taken into account for the control points in the leeward part of the rotor.

Notice that the term $\arccos(y)$ always evaluates to a positive angle, therefore, for the leeward part of the rotor the $*$ and $**$ terms can be written as:

$$-Q_n(\arccos(y))^* = -Q_{n,(N-j-1)} \tag{4.25}$$

$$Q_n(-\arccos(y))^{**} = Q_{n,j} \tag{4.26}$$

Therefore, for a control point located at $\theta = 355°$, $-Q_n(\arccos(y))$ will become $-Q_n(5°)$ and $Q_n(-\arccos(y))$ will become $Q_n(355°)$. Li [19] suggests to write equations 4.21 and 4.22 in matrix form:

$$w_{x,j} = -\frac{1}{2\pi}\sum_{i=0}^{N-1}Q_{n,i}C_{x,j,i} - (Q_{n,N-j-1})^* + (Q_{n,j})^{**} \tag{4.27}$$

$$w_{y,j} = -\frac{1}{2\pi}\sum_{i=0}^{N-1}Q_{n,i}C_{y,j,i} \tag{4.28}$$

The $C_{x,j,i}$ and $C_{y,j,i}$ are the so-called influence coefficients and they represent the integral terms in equations 4.21 and 4.22 . Notice that these influence coefficients depend only on geometrical properties, time is saved by precomputing the influence coefficients before even beginning the numerical solution.

4.1.1   The normal and tangential loads

The above equations for the perturbation velocities depend on geometrical properties –which can be known beforehand– and the normal loads Q_n. In order to compute the loads, it is necessary to draw upon the blade-element theory. Firstly, the aerodynamic properties must be known in order to compute the forces acting on the blade.

Figure 4.2 depicts the velocities acting on the aerodynamic center of the blade at position θ. The free stream velocity V_∞ (coming from the left) is broken down into its x and y components so that they can be projected along the blade's tangential and normal axes. Note that α is the angle of attack with respect to the blade's chord, ωR is the tangential velocity of the blade due to rotation, V_t and V_n are the tangential and normal velocities, V_{rel} is the relative velocity (units in $\frac{m}{s}$) and δ is the pitch angle which is formed between the blade's chord and the tangent of the flight path of the turbine.
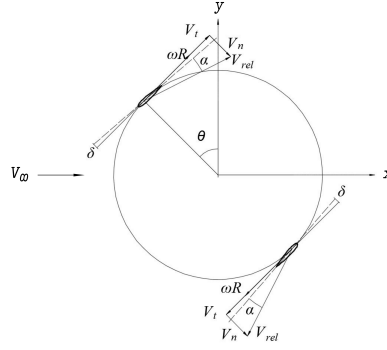
Figure 4.2: *Velocity triangle of a blade element.*

With the aforementioned explanation it is now possible to state that the projections of the free stream velocity will depend upon the perturbation velocities:

$$V_x = V_\infty(1 + w_x) \tag{4.29}$$

$$V_y = V_\infty w_y \tag{4.30}$$

Here, only equation 4.29 contains the unit added inside the parenthesis because the free stream velocity is assumed to be in the x direction only.
The tangential and normal velocities –assuming counterclockwise rotation– are:

$$V_t = V_x \cos\theta + V_y \sin\theta + \omega R \tag{4.31}$$

$$V_n = V_x \sin\theta - V_y \cos\theta \tag{4.32}$$

The relative velocity, that is, the velocity seen by the blade is given by:

$$V_{rel} = \sqrt{V_t^2 + V_n^2} \tag{4.33}$$

The angle of attack can be derived from simple trigonometry:

$$\alpha = \arctan(V_n/V_t) - \delta \tag{4.34}$$

The widely accepted Reynolds number for a blade element and its correspondent lift and drag forces are:

$$Re_b = \frac{V_{rel} \cdot c}{\nu} \tag{4.35}$$

The characteristic length is the turbine's blade chord denoted by c. The blade lift and drag forces at a specific location are:

$$L = \frac{1}{2}\rho c V_{rel}^2 C_L \tag{4.36}$$

$$D = \frac{1}{2}\rho c V_{rel}^2 C_D \tag{4.37}$$

The force coefficients can be extracted from data of wing profiles by performing a look-up method based on the angle of attack and the local Reynolds number. The normal and tangential forces with respect to the blade's chord are projected in the following manner:

$$F_n = L\cos\alpha + D\sin\alpha \tag{4.38}$$

$$F_t = L\sin\alpha - D\cos\alpha \tag{4.39}$$

The forces of main interest are the normal and tangential ones with respect to the cylinder's surface, this tangential force is responsible for generating the wind turbine's torque. Figure 4.3 shows the projection of these forces.
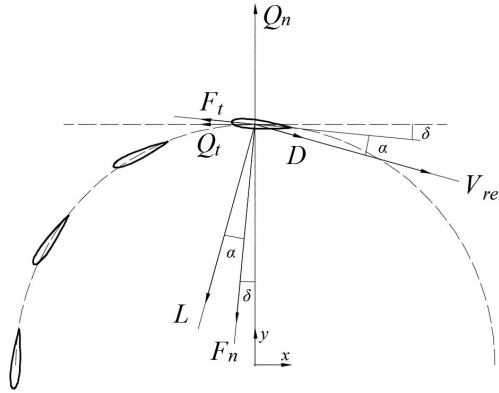
Figure 4.3: *Aerodynamic forces acting on the blade Note that F_n is normal to the blade's chord while Q_n is normal to the blade's flight path.*

Taking into account that the turbine has N_B blades, the instantaneous normal and tangential forces of each blade with respect to the flight's path can be modeled as:

$$Q_n(\theta_k) = (F_n(\theta_k) \cos \delta - F_t(\theta_k) \sin \delta) \frac{1}{1/2 \rho V_{rel}^2 c} \tag{4.40}$$

$$Q_t(\theta_k) = - (F_n(\theta_k) \sin \delta + F_t(\theta_k) \cos \delta) \frac{1}{1/2 \rho V_{rel}^2 c} \tag{4.41}$$

Where k is the index for the *k-eth* blade and each blade will be set appart from the others by $360°/N$ degrees, δ is the pitch angle of the blade.

Since this is a steady-state problem, all variables must be multiplied by the N_B blades, time averaged in one revolution by $2\pi R$ and non-dimensionalized by ρV_∞^2; therefore the loads become:

$$Q_n(\theta) = \frac{N_B}{2\pi R \rho V_\infty^2} (F_n(\theta) \cos \delta - F_t(\theta) \sin \delta) \tag{4.42}$$

$$Q_t(\theta) = -\frac{N_B}{2\pi R \rho V_\infty^2} (F_n(\theta) \sin \delta + F_t(\theta) \cos \delta) \tag{4.43}$$

4.1.2   Normalization of the loads

The previous set of equations depend on variables with their correspondent dimensions. It is a good practice, though, to non-dimensionalize (normalize) all of the equations in such a way that they only depend on other non-dimensional variables; thus, the velocities are normalized by the quantity V_∞:

$$v_x = 1 + w_x \tag{4.44}$$

$$v_y = w_y \tag{4.45}$$

$$v_n = v_x \sin \theta - v_y \cos \theta \tag{4.46}$$

$$v_t = v_x \cos \theta + v_y \sin \theta + \lambda \tag{4.47}$$

The rotational speed of the rotor normalized by V_∞ is $\omega R / V_\infty$, a common characteristic parameter of wind turbines called the *tip-speed ratio* which is denoted by λ or TSR. The normalization of the relative speed and the angle of attack is as follows:

$$v_{rel} = \sqrt{v_t^2 + v_n^2} \tag{4.48}$$

$$\alpha = \arctan(v_n/v_t) - \delta \tag{4.49}$$

The aerodynamic forces become:

$$C_n = C_L \cos \alpha + C_D \sin \alpha \tag{4.50}$$

$$C_t = C_L \sin \alpha - C_D \cos \alpha \tag{4.51}$$

Equations 4.42 and 4.43 become:

$$Q_n(\theta) = \frac{\sigma}{2\pi} v_{rel}^2 (C_n(\theta) \cos \delta - C_t(\theta) \sin \delta) \tag{4.52}$$

$$Q_t(\theta) = -\frac{\sigma}{2\pi} v_{rel}^2 (C_n(\theta) \sin \delta + C_t(\theta) \cos \delta) \tag{4.53}$$

The turbine's solidty is given by $\sigma = N_B c / 2R$, which can be seen as the blades' area per unit length divided by the turbine's swept area per unit length.

4.2 Actuator Cylinder Tangential Loads Modification

At the beginning of the chapter, it was stated that the non-dimensional volume forces f_x and f_y were a projection of the normal forces f_n acting on the surface of the cylinder, the tangential forces f_t were neglected. Cheng [20] devised a modification of the actuator cylinder model by including the terms f_t. See Appendix A for the derivation of the corresponding equations. The modified equations for the perturbation velocities are similar in nature:

$$
\begin{aligned}
w_{x,j} = & -\frac{1}{2\pi}\sum_{i=0}^{N-1} Q_{n,i}C_{x,j,i} - \frac{1}{2\pi}\sum_{i=0}^{N-1} Q_{t,i}C_{y,j,i} - (Q_{n,N-j-1})^* + (Q_{n,j})^{**} \\
& -\frac{y_i}{\sqrt{1-y_i^2}}(Q_{t,N-j-1})^* - \frac{y_i}{\sqrt{1-y_i^2}}(Q_{t,j})^{**}
\end{aligned}
\tag{4.54}
$$

$$
w_{y,j} = -\frac{1}{2\pi}\sum_{i=0}^{N-1} Q_{n,i}C_{y,j,i} + \frac{1}{2\pi}\sum_{i=0}^{N-1} Q_{t,i}C_{x,j,i}
\tag{4.55}
$$

4.3 Verification of the model

To ensure the proper functioning of the model, a code in Python was elaborated. The results of Ang Li [19] were used to compare the results of the present work and those of his.
An NACA0015 inviscid airfoil polar was used, although data from viscous NACA profiles could be used as well. The following are the lift and drag coefficient respectively:

$$
C_L = 2\pi \cdot 1.11 \sin\alpha
\tag{4.56}
$$

$$
C_D = 0
\tag{4.57}
$$

Figures 4.4 and 4.5 shows the variation of the thrust and power coefficients with respect to the wind turbine's solidity at various tip-speed ratios. See Appendices B and C for the derivation of the thrust coefficient and the power coefficient respectively.
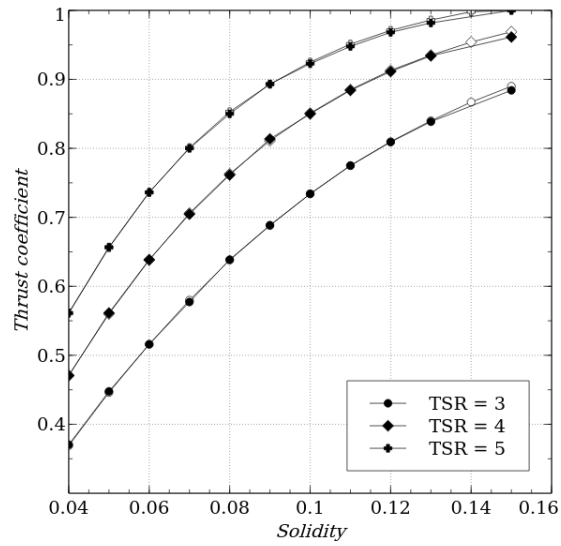
Figure 4.4: *Comparison of the thrust coefficient curves. White symbols are from this work, black dots are from Li [19].*
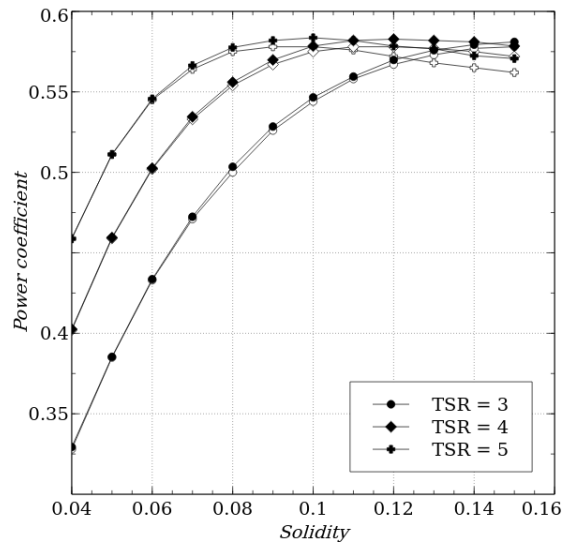
Figure 4.5: *Comparison of the power coefficient curves. White symbols are from this work, black dots are from Li [19].*

Evidently, there is a good agreement between both results. The reason why the power curves get too close to the Betz limit is that the chosen airfoil polar is inviscid and the correspondent function for the lift coefficient actually delays stall, thus, the lift coefficient doesn't drop prematurely as in the case of a viscous airfoil polar. Next, the comparison of local non-dimensional variables (perturbation velocities, loads, angle of attack and relative velocity) and their variation along the cylinder's surface is presented.
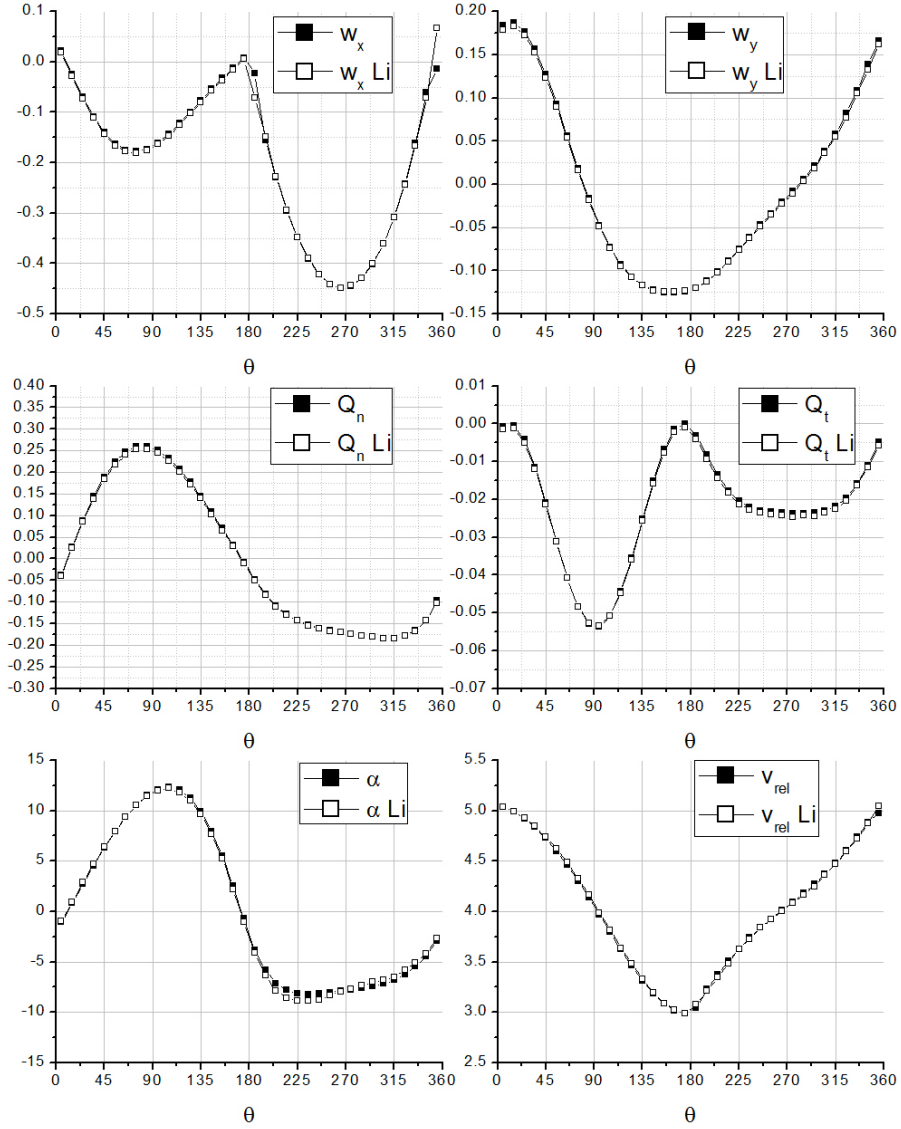
Figure 4.6: *Validation for the case of a wind turbine with $\lambda = 4$, $\sigma = 0.07$, $N_B = 2$, mounted at the aerodynamic center $1/4c$. The black dots belong to the present work.*

It can be seen from Figure 4.6 that the values of the perturbation velocities in the windward

zone —0°–180°— are lower than the values in the leeward zone, this implies that most of the energy is extracted in the windward zone as it can be observed in the Q_t subplot, where the non-dimensional tangential load reaches higher values in the windward zone.

4.4   Conclusions

The actuator cylinder model was successfully implemented in Python. The correction factor was used according to Madsen, Larsen, Vita and Paulsen [21]. The execution time in a desktop computer doesn't exceed 0.9 seconds, which is ideal for investigating the influence of parameters such as tip-speed ratio, solidity, number of blades, pitch angle, on the overall performance of the turbine. Important variables such as perturbation velocities, drag and lift coefficients, angle of attack, normal and tangential loads, power and thrust coefficient were able to be studied with the present model. It is important to stress out the fact that the model works fine only on low solidity rotors –low chord-to-radius ratio or a large number of blades–; the solidity is defined as the quotient of the area of the blades and the swept area of the rotor.

Chapter 5

RANS-AC Model

5.1 Introduction

This section proposes an actuator model integrated within an OpenFOAM solver that relies on replacing the turbine by volumetric forces exerted on the fluid, this approach eliminates the need of highly resolved meshes around the blades, thereby reducing the mesh size considerably. The forces are modeled using the steady-state actuator cylinder model [6], although any other model can be employed. This approach is two-dimensional and the computational time needed for simulating a wind farm ranges from minutes to hours; moreover, the fidelity is superior to that of simple momentum models since the viscous wake is resolved by the RANS simulation. This proposed model provides the capability of serving as an optimization tool for vertical-axis wind turbine farms.

The current RANS-AC has the potential of modeling entire wind farms without relying on empirical corrections for the wake or without the need of HPC (high performance computing). Moreover, only simple input data must be entered, namely the geometrical and operational parameters and inlet boundary conditions for the simulation.

5.2 AC validation against a 1.2 kW Windspire turbine

The Windspire turbine [16] was chosen for validation because it will be used throughout this work (it is the turbine employed in the only wind farm experiment available), therefore the results of the AC model will be compared against experimental data. Ideally, it would be better to validate against a low-solidity turbine since it meets the requirements of the AC model; nevertheless the Windspire turbine will be used despite it having a solidity of $\sigma = 0.32$. According to [16], the turbine is kept at an optimal tip-speed ratio $\lambda = 2.3$ up until 10.6 m s^{-1}, after this point the rotational speed is kept constant and λ begins to decrease. The turbine's radius is $R = 0.6$ m, the height is $H = 6.1$ m, the number of blades is $N = 3$, the chord is $c = 0.128$ m and the airfoil is a DU06W200 section derived from a NACA0018 section, except the maximum thickness is 20% and little camber is added.

The turbine σ is given by $\sigma = N_B c / 2R$, which can be interpreted as the blades' area per unit length divided by the turbine swept area per unit length. It is important to keep σ low, otherwise the basic assumptions about the model break down since effects such as flow curvature and flow distortion are not taken into account. The model does not guarantee any results whatsoever if high-solidity rotors are used. [22, p. 40] uses the AC model in his Ph.D. thesis and the solidity values encountered there are fairly low –around 0.12 for a large two-bladed VAWT–; [5, p. 169] also employs low-solidity turbines in the development of his double multiple stream-tube model,

the values of σ do not go beyond 0.22. The problem of solidity becomes important in small turbines as they have a large c/R ratio. According to [23], these blades are subjected to a curvilinear flow which alters the boundary layer of the airfoil. Kinematic analysis from [23] also shows that the angle of attack and the relative wind velocity are dependent on the azimuthal angle, the tip speed ratio and the chord-to-radius ratio; therefore α and v_{rel} can vary significantly chordwise since any point on the blade has a unique radial distance. By employing conformal mapping techniques, it is possible to transform the airfoil in the curvilinear flow to a virtual airfoil in a rectilinear flow. The transformation introduces a camber and an additional angle of incidence –namely virtual camber and virtual incidence– which are also dependent on the azimuthal angle, although they can be averaged by the mean value of one revolution. Thus it is shown in [23] that these virtual airfoils have lift at $\alpha = 0$, therefore the C_L vs α curve is shifted upwards depending on the value of c/R. Not only the lift coefficient is affected but also the stall angle, which occurs much earlier as in the original airfoil without camber; this premature stall deteriorates the efficiency of the wind turbine. Results from wind turbines with values of $c/R = 0.114$ and $c/R = 0.26$ each in [23] show that the power coefficient is strongly dwindled as c/R increases. In summary, results from the AC model using relatively high-solidity wind turbines will certainly miscalculate the angle of attack to a certain degree, thus overestimating the power coefficient of the turbine.

A particular challenge was to find polars for the DU06W200. [24] provides both theoretical and experimental data for Reynolds numbers of 300,000 and 500,000 but does not give information whatsoever for Reynolds number below 300,000, the turbine's global Reynolds number at $8 \, \mathrm{m\,s^{-1}}$ is $Re = R\omega c/\nu = 130,000$, ω being the rotational speed. It was then decided to use polars from the software QBlade [25] which is based on a vortex panel code derived from the MIT's code Xfoil [26]. QBlade is able to predict both drag and lift coefficients at angles of attack below stall, for ranges above stall, an extrapolation can be done based on the Montgomerie model, which is more accurate (at least in this case) than the Viterna model. It was observed that the Montgomerie model predicted better the shear drop in lift after stall has occurred. Figures 5.1 and 5.2 show the polar for both the lift and drag coefficient at the typical Reynolds numbers encountered by this turbine; QBlade seems to have trouble at low Reynolds numbers, instabilities are manifested in the zone just before stall plus the fact that the slope before stall is not always linear and presents jagged segments, despite the shortcomings, polars at $Re = 50,000$ $Re = 100,000$, $Re = 150,000$ and $Re = 200,000$ were included. At higher Re it was found that QBlade overestimated lift and could not predict well the shear drop of lift after stall according to wind tunnel data from [24].

No attempt was made to introduce dynamic stall or flow curvature effects. Dynamic stall models can conflict with the AC model according to [19]. As for flow curvature due to the turbine's $c/R = 0.21$, –which is above 0.075 and 0.11 in [5, p. 169] and [22, p. 40], respectively–, it was decided not to employ any model due to the increase in computational cost. [19] uses Migliore's model which computes the shape of a virtual airfoil with added camber (the original airfoil in a curved flow is mapped to a cambered airfoil in a straight flow); consequently, the lift and drag coefficients have to be recomputed according to the shape of the virtual airfoil, this needs models such as the vortex panel model which can be expensive considering that the panel model has to be called for every azimuthal position times the number of iterations.
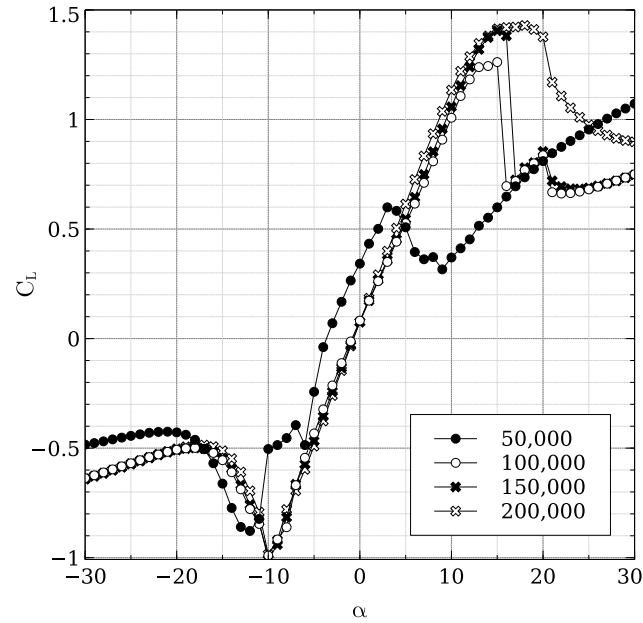
Figure 5.1: Lift polar for the DU06W200 airfoil at different Re.
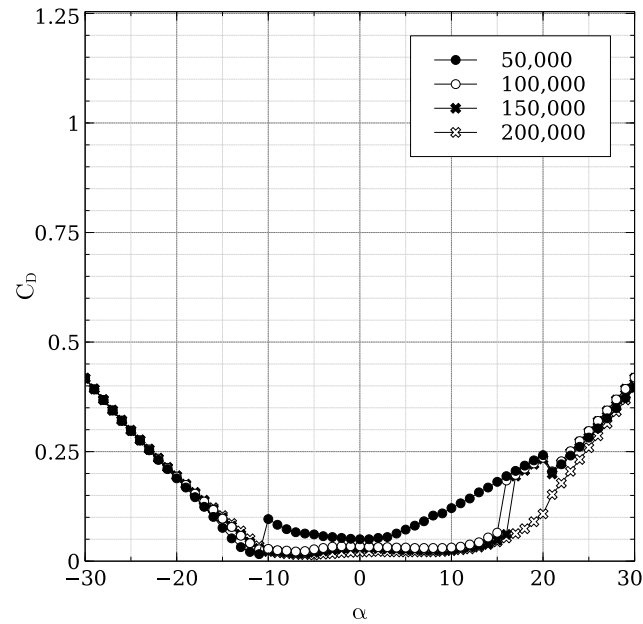
Figure 5.2: Drag polar for the DU06W200 airfoil at different Re.

The results from the AC model were compared against data from an AC model results provided by [27], experimental data is also available. Figure 5.3 shows how both AC models overpredict the C_P. This overestimation must be in part because both AC models employ limited polars, e.g. [27] using wind tunnel data at $Re = 300,000$ and this work using data ranging from

$Re = 50,000$ to $Re = 200,000$; thereby neglecting the fact that at lower wind speeds Re is much lower. The other reason must be because of the fact that the model is only two-dimensional and no effects from struts, tower, tip losses, as well as flow curvature and dynamic stall are included. There is an overall good tendency, the results from the current work and the experimental data both peak at 10 m s^{-1}. Without accurate polars from wind tunnel measurements, it is hard to get accurate results, the C_P is therefore very sensitive to the polars and care must be taken when interpreting the lift and drag coefficients.
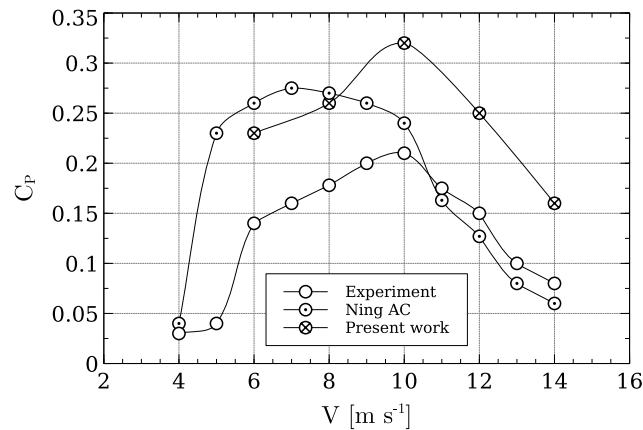
Figure 5.3: 1.2 kW Windspire turbine validation and comparison. λ is kept at 2.3 up until 10 m s^{-1}.

5.3   RANS-AC implementation

The AC model can be incorporated into one of the OpenFOAM solvers by taking advantage of the source terms in the Reynolds-averaged Navier-Stokes equations. The solver used is called *simpleFoam* [28] which solves the steady-state incompressible Navier-Stokes equations for turbulent flows. A new solver called *actuatorCylinderSimpleFoam* was made by the author of this thesis using the *simpleFoam* solver as a template. Whereas the solver needs minimal modification, the AC routines took most of the work. These routines are placed in separate files. The k-ϵ turbulence model is preferred since it has proven to yield relatively good results in environmental flows such as wakes [29, 30]. Algorithm 1 shows the process followed by the new solver.

Algorithm 1 actuatorCylinderSimpleFoam solver implementation

   Create volumetric field
   Read coordinates
   Read geometrical and operational parameters
   for $i \leftarrow 1$ to N **do**
      Create an actuator cylinder $\{i$ is the current cylinder$\}$
      Identify cells that belong to the cylinder
      Initialize arrays of velocity and volumetric forces of current cylinder
   end for
   repeat
      Solve for velocity
      Clear volumetric field
      for $i \leftarrow 1$ to N **do**
         Add Force(mesh, U, volumeForce)
         $\{$Access the mesh and the velocity field $U.\}$
         $\{$Read the velocities in the corresponding cells.$\}$
         $\{$Execute AC and compute forces.$\}$
         $\{$Apply forces in the cylinder's cells of volumetric force field.$\}$
      end for
      Pressure correction
   until convergence is achieved **or** last time step is achieved

---

Notice that N is the number of cylinders (turbines), each cylinder has a set of corresponding cells where the velocity is read and then passed to the AC routine which computes the volumetric forces and passes them back to OpenFOAM using the function *Add Force*. The thickness of the cylinder is subjective and it will be explained in the next sections. The way the volumetric forces are calculated by the RANS-AC is by assuming that they do not vary significantly across the thickness of the cylinder, therefore Eq. 4.1 becomes Eq. 5.1, where Δr is the thickness of the cylinder and $f_n(\theta)$ are the volumetric forces normal to the cylinder as a function of the azimuthal angle. These normal forces have to be projected in the x and y direction of the volumetric field of the simulation.

$$f_n(\theta) = Q_n(\theta)/\Delta r. \tag{5.1}$$

5.3.1 RANS-AC verification against AC model

In order to prove that the RANS-AC has been implemented correctly, the power coefficient of the RANS-AC will be compared against that of the stand-alone AC model. A sensitivity analysis concerning the thickness of the cylinder and the turbulence intensity I at the inlet of the domain will be discussed. A uniform mesh was chosen for simplicity. Although OpenFOAM is provided with mesh refinement utilities, the refined mesh is inevitably three-dimensional due to the meshing algorithm, which is even more computational expensive, therefore the refined mesh was discarded. The boundary conditions are inlet, outlet, top and bottom, back and front. Table 5.1 shows the boundary conditions for every variable OpenFOAM has to compute. Numerical schemes can be found in Appendix E.

Boundary conditions						
	U	p	$volForce$	k	ϵ	ν_T
inlet	freestream	zeroGradient	fixedValue	freestream	freestream	calculated
outlet	zeroGradient	fixedValue	fixedValue	freestream	freestream	calculated
top/bottom	freestream	freestreamPressure	fixedValue	freestream	freestream	calculated
front/back	empty	empty	empty	empty	empty	empty

Table 5.1: Boundary conditions at time 0 for the computational domain.

It must be cleared that the *simpleFoam* solver interprets p as p/ρ since the RANS equations are divided by ρ due to the flow being incompressible. Free stream conditions acts like a zero-gradient condition when the flow comes out of the domain and acts like a fixed value when it is not; it is a kind of inlet/outlet condition in case of having flow reversal. The *freestreamPressure* is an outlet-inlet condition that uses the velocity orientation to act either as a zero-gradient condition or a fixed-value condition. The empty boundary condition means that nothing is calculated at those faces, this is only valid for two-dimensional cases with one cell in the third direction.

In summary, all variables have to be initialized at time 0 in the domain. In order to initialize the values of all variables, a set of equations is needed. Eqs. 5.3, 5.4, 5.5 and 5.5 are the turbulence length scale, the turbulent kinetic energy, the turbulent kinetic energy dissipation rate and the turbulent viscosity; respectively. The least intuitive is l, this value is taken from [31, p. 66] based on the case of a wake flow, where L is the wake width which will be taken as the diameter of the cylinder. C_m is just a model constant set to 0.09 by default, it is used in isotropic turbulent flows.

$$l = 0.08L, \tag{5.2}$$

$$k = 1.5(\|\vec{U}\|I)^2, \tag{5.3}$$

$$\epsilon = \frac{C_m{}^{0.75}k^{1.5}}{l}, \tag{5.4}$$

$$\nu_T = \frac{C_m k^2}{\epsilon}. \tag{5.5}$$

The RANS-AC was verified against the Windspire turbine using a fine mesh and a coarse mesh. The mesh size was based on enclosing the cylinder in a $n \times n$ cell square, the rest of the domain was meshed accordingly. Distances from the inlet to the turbine could range from 3 D to 5 D (diameters) as well as distances from the turbine to the sides. Distances from the turbine to the outlet could be shorter than 10 D. No impact was observed in the C_P. Table. 5.2 shows the comparison of the power coefficients as well as the mesh parameters. No significant difference was observed between both meshes, although both meshes underpredicted C_P at 14 m s^{-1}. The number of time steps is dependent of the inlet velocity, e.g. the wake takes longer to develop when the inlet velocity is low. Although the wake development depends strongly on the inlet velocity and the value of ϵ, the power coefficient reaches a stable value much earlier. This is verified in a log file. The development of the wake can be observed visually by inspecting each time step; at 8 m s^{-1}, 800 time steps were sufficient to achieve the final shape of the wake and a steady power coefficient.

The distance from the turbine to the outlet does not seem to affect the result. In this case, the outlet was placed 10 D away from the turbine. Care must be taken when choosing the value of I, data from the wind farm experiment[10] was used to compute the value of I. Observations

taken every 10 minutes from several wind directions and velocities were extracted; e.g. for 8 m s^{-1}, data from velocities ranging from 7 m s^{-1} to 9 m s^{-1} were collected, then the mean of the quotient of the standard deviation and the average velocity was calculated. The same process was done for the rest of the velocity bins.

		Mesh sensitivity results		
	stand-alone AC	**fine mesh**	**coarse mesh**	
		1.0 chord thickness cylinder	1.5 chord thickness cylinder	
		50×50 cell enclosing square	30×30 cell enclosing square	
U_∞	C_P	C_P	C_P	I
4	0.22	0.196	0.197	0.130
6	0.23	0.216	0.217	0.125
8	0.26	0.275	0.270	0.134
10	0.32	0.339	0.340	0.116
12	0.25	0.230	0.230	0.110
14	0.16	0.100	0.084	0.106

Table 5.2: RANS-AC results from two different meshes verified against the stand-alone AC.

Since a volumetric field is created initially, at the end of the simulation it is possible to visualize these forces using Paraview (a postprocessing application). Figure 5.4 shows the volumetric forces acting on the counter-clockwise rotating cylinder at 8 m s^{-1} (coarse mesh). It is reminded that the volumetric field is a vector field but the magnitude is a scalar.
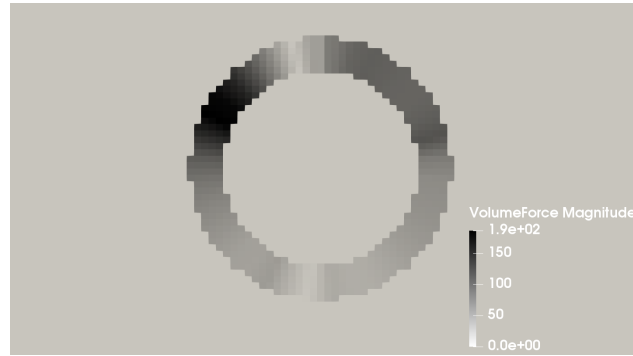
Figure 5.4: Volumetric forces acting on the cylinder. Flow goes from left to right. Free stream speed is 8 m s^{-1}, coarse mesh.

5.4 Validation against experimental results

This section is meant to test the capabilities of the RANS-AC in a multi-turbine environment. Experimental data from a small wind farm of VAWTs was found in [10]. These kinds of experiments are hard to find in the literature since most experimental studies on VAWTs are done on one turbine only. The experiment consists of a set of turbines that can be rearranged in any fashion in order to test the performance of several layouts, the location is in the Antelope Valley, California. The turbines are the same 1.2 kW Windspire turbines mentioned in the

past sections. Although data for multiple wind turbine arrays are available, only data from two different arrays will be used here, namely an array of 4 turbines and another array of 18 turbines. Figures 5.5 and 5.6 show the layouts of the two arrays. The eighteen-turbine arrays has counter-clockwise rotating turbines. It is said in [10] that the most prevalent wind direction is from the southwest, therefore the turbines in Figs. 5.5 and 5.6 were aligned in that direction. The wind speed is about 8 m s^{-1} and λ is kept at 2.3. The value of I is set to 0.13 according to Table 5.2.
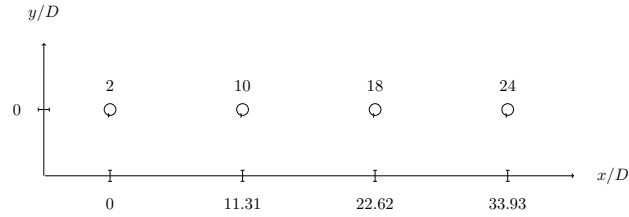
Figure 5.5: Four turbines in a row. The distance from turbine to turbine is 11.31 D (diameters). Flow is from left to right.
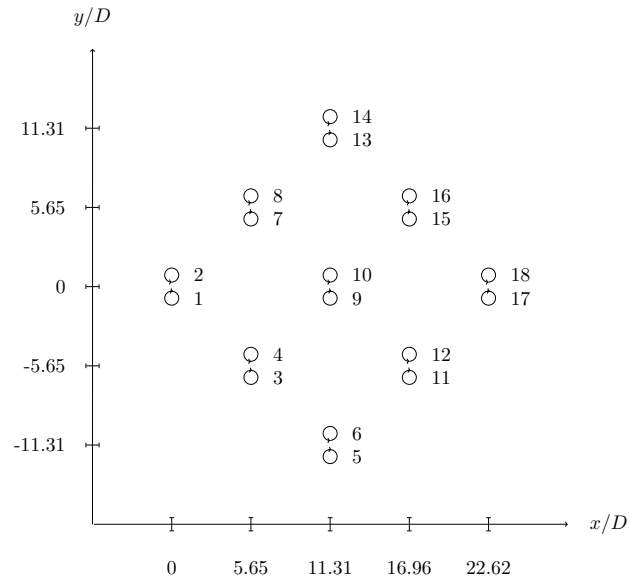
Figure 5.6: Fish schooling configuration. Turbines are placed in a counter-clockwise rotating fashion. The flow is also from left to right.

5.4.1   Model calibration

Since the numerical simulation must be provided with the turbulence length scale in order to compute the turbulent kinetic energy dissipation rate at the inlet, a study on the width of the wake was conducted in order to find the appropriate turbulence length scale. The results in Table 5.1 were obtained supposing that the width of the wake was similar to the diameter of the turbines. This did not impact the results of the C_P; however, it was observed that the

streamwise development of the wake was sensitive to this value, this is reflected in ϵ since it depends on $l = 0.08L$ where L is the width of the wake.

In order to obtain a value for l, a simulation with $L = D$ was run and the width of the wake was found. Care must be taken in selecting the width of the wake as it varies downstream. It was decided to take the value at 7 D, roughly; the reason for this is that the rate of growth begins to reach a steady value. The rate of growth of the wake at small distances downwind cannot be neglected. At larger distances the wake begins to fade away and a wake width is hard to define. This is exemplified in Fig. 5.7, the procedure consisted in placing several downwind stations, e.g. crosswind plots of the magnitude of the velocity. The width was then measured from end to end, where each end has a velocity value of the free stream velocity, which is 8 m s^{-1} in this case. These ends can be found visually by intersecting the wake plot with a horizontal line drawn at $U = 8 \text{ m s}^{-1}$, where U is the magnitude of the velocity. Notice in the figure that the location at which the ends of the wake stop varying is at 7 D approximately. The width is then $y^+ - y^-$ where y^+ is the upper end and y^- is the lower end. It is also interesting to notice the skewness of the wake, since the turbine is rotating counter-clockwise, most of the power is extracted in the positive portion of y.
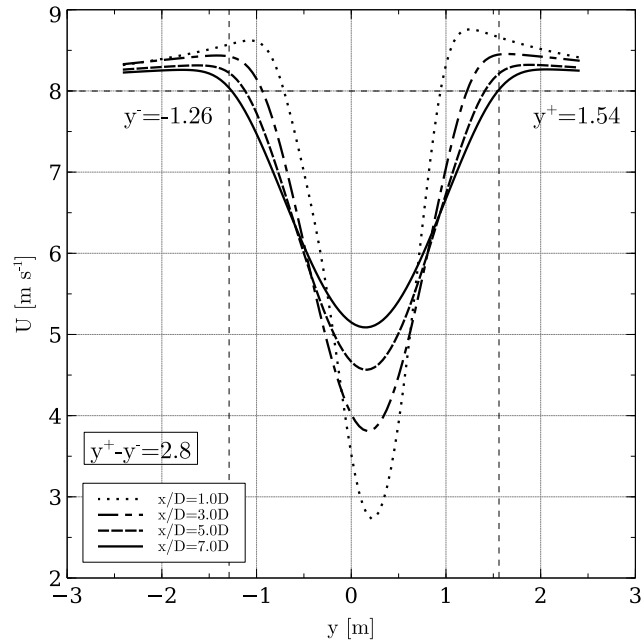
Figure 5.7: Wake width at different downwind stations. The width begins to reach a stable value 7 D and its value is 2.8 m.

Once the new value of L was found, an iterative procedure following the same logic was conducted: a new simulation with $L = 2.8$ was conducted and the width of the wake was obtained in the same fashion. The procedure was stopped when the width stop varying across iterations. Figure 5.8 shows the final value of the width of the wake, which is 3.7 m, the turbulence length scale is found by substituting 3.7 in $l = 0.08L$.
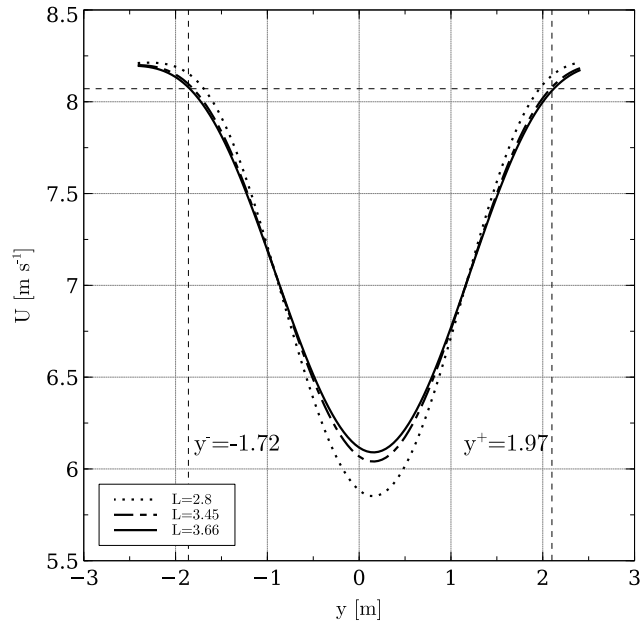
Figure 5.8: Wake widths obtained by following an iterative procedure. All the plots are located at 7 D downwind.

5.4.2   Array of 4 turbines

The power coefficients from this array were obtained from data published by [10]. The distance from turbine to turbine is 11.31 D. Figure 5.9 shows the C_P and the normalized C_P. The latter was taken to be the current turbine C_P divided by the leading turbine C_P; experimental data was normalized with the leading turbine's experimental C_P and numerical data was normalized accordingly. There is a clear overestimation of the C_P, as discussed earlier, the AC model tended to overestimate the C_P of this particular turbine. The normalized C_P shows that there is an overall good trend: the power coefficients decrease in the same manner.
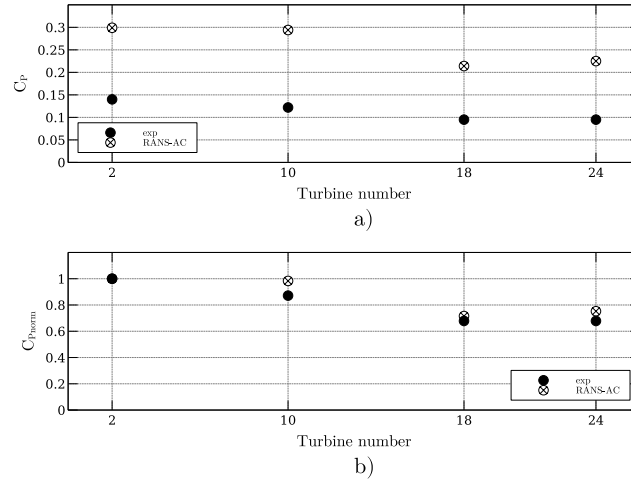
Figure 5.9: Power coefficients of the four-turbine array. a) is the actual C_P and b) is the normalized C_P.

Another plot concerning the velocity and turbulence intensity along the center line is included in Fig. 5.10. The magnitude of the velocity is normalized with respect to the free stream velocity U_∞. The value of I was calculated in Paraview by creating a new field according to the following equation derived from Eq. 5.4.

$$I = \frac{\sqrt{(2/3)k}}{\|\vec{U}\|}.$$ (5.6)

The RANS-AC underestimates the wake recovery in between the turbines. The value of I starts at 0.13 according to Table 5.2, then it reaches a steady pattern past the second turbine, values up to 0.4 can be found near the wake of each turbine. Although there are no experimental data to compare with, the value of I along the center line follows an expected pattern and it decays almost to its original value past the last turbine.
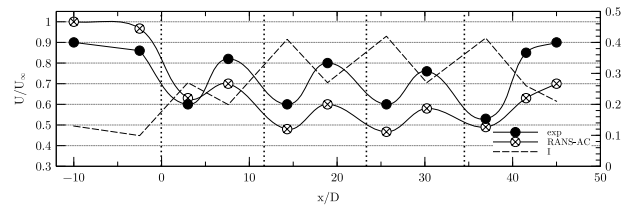
Figure 5.10: Wake across the turbine array. The axis for I is located at the right side of the plot. Vertical dotted lines signify the locations of each turbine.

5.4.3 Array of 18 turbines

A plot similar to Fig. 5.9 is presented for this case. The C_Ps across the array do not follow a coherent pattern, e.g. turbines that have been blocked present similar or even higher C_Ps than the turbines free of blockage. Figure 5.11 shows the current C_P in a) and the normalized C_P in b). The normalized C_P was obtained by dividing each C_P by the maximum C_P.
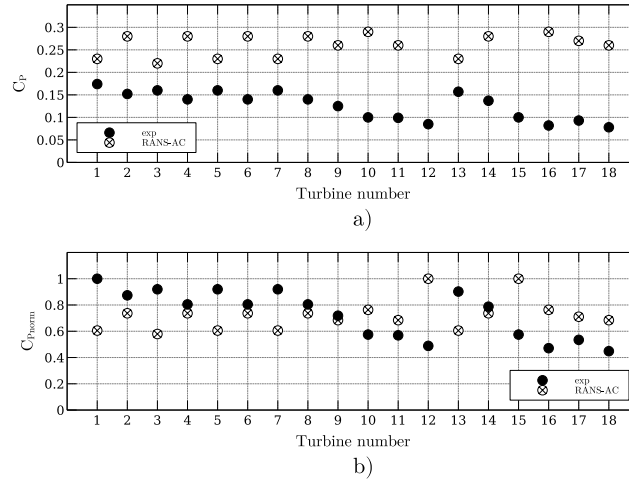
Figure 5.11: Power coefficients of the eighteen-turbine array.

It was observed that a portion of the angles of attack of the turbines that were free of blockage were above stall according to Fig. 5.1. This is wrong since the manufacturer states that the turbine is kept at an optimal λ of 2.3, therefore meaning that it is not stalled. As the flow traverses each turbine downwind, it loses momentum, therefore each blocked turbine sees lower relative velocities and thus lower angles of attack. It would be intuitive to think that lower angles of attack lead to lower lift coefficients, but since the turbine is stalled, the lift coefficients might be even higher than those in the stalled regime. Data extracted from a row of turbines in the array is presented in Fig. 5.12. The plot shows the angles of attack and lift coefficients from turbines 2, 10 and 18. It can be seen that there is indeed a decrease in the amplitude of α as each turbine presents blockage from another turbine; however, it is important to notice that in this case, turbine 18 for instance, has the lowest amplitude of α but its coefficients are not in the stall region where they drop sharply, therefore achieving higher lift and tangential force coefficients. The local Re ranges from 100,000 to 200,000 and the positive stall angle of attack is about 16 ° according to Fig. 5.1. Turbine 18 has a maximum positive α of 13 °, therefore it operates at an optimal regime, which should not happen actually.

It must be clear that this fault is due to the wrong predictions of α in the AC model no due to the OpenFOAM solver, which is possible in case high-solidity turbines are being used. The incoherent pattern of C_Ps along a row of turbines did not occur in the case of the array of 4 turbines. It is thought that this array was not affected by the accelerated flow in between turbines as in the case of the array of 18 turbines; therefore the velocity across the center line decayed faster and the turbines in the back rows operated in a regime well below stall, achieving even lower C_Ps.
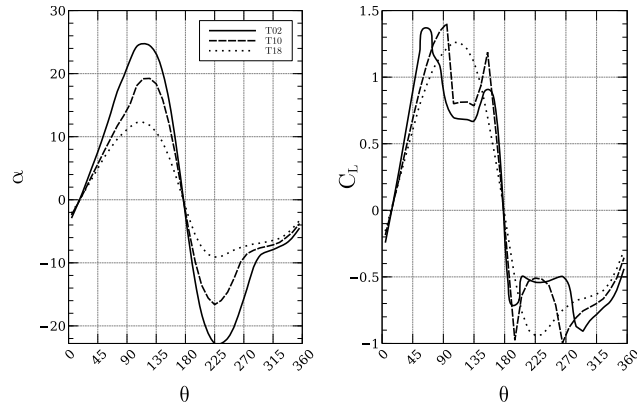
Figure 5.12: α and C_L from turbines T02, T10 and T18.

5.5 Verification with an LES simulation

As seen in Section 5.4, the case of the eighteen-turbine wind farm did not yield good results mainly because of the inability of the AC model to correctly predict angles of attack for high-solidity turbines. In seeing this, an additional verification study was done to prove that the RANS-AC does work well indeed if low-solidity turbines are used. The work from [1] is used as a reference. An LES simulation was carried out on a three-bladed VAWT with a radius of 25 m, a chord of 1.5 m, and a height of 100 m. The wing's cross section is an NACA0018. The rotational speed is 16.5 rpm and the wind speed is 9.6 m s^{-1}, thus yielding a tip-speed ratio of 4.5. The turbulence intensity value at the inlet is 0.083 and an atmospheric boundary layer is used, although this is not possible in a 2D simulation. Figure 5.13 shows a C_P plot against λ. The current RANS simulation was done a cylinder thickness of 2 chords and an enclosing square of 30×30 cells. Although the RANS-AC model overpredicts the value of C_P, there is a very good agreement on the trend of the curve. Results from the stand-alone AC model are presented too.
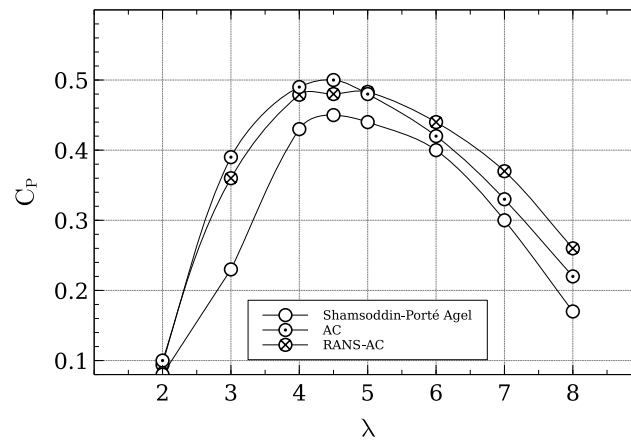
Figure 5.13: Comparison of C_P results from an LES simulation with the current RANS-AC. Turbine's σ is 0.09.

Next, a comparison of the wake of the turbine is presented. The LES wake is taken at the equator. The width of the wake L was taken as the diameter of the turbine and the iterative procedure done in Section 5.4 was not done since the results using the diameter as the width of the wake were satisfactory. The accurate width of the wake seemed to impact mostly the initial value of ϵ (which depends on $l = 0.08L$) at the inlet and not much difference was observed in the wake recovery when using the diameter as the width of the wake. Figure 5.14 shows very good agreement in the development of the wake.
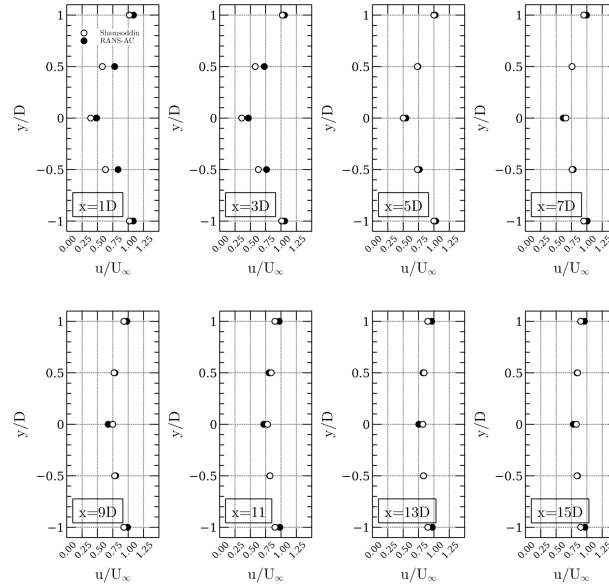
Figure 5.14: Comparison of the LES wake at different downwind distances with the current RANS-AC results.

Finally, the same eighteen-turbine wind farm simulation is done, except this time the turbine from [1] is used. The relative distances from turbine to turbine are preserved. The Reynolds number could not be preserved because that would imply to run the turbine at extremely low wind speeds and extremely low rpm. The purpose is to show that the RANS-AC has no trouble predicting the right trend of the power coefficients when using low-solidity turbines. The solver converged at 1564 iterations, although the power coefficients reached an almost constant value at 1000 iterations. Roughly an hour had passed by the time the solver reached 1000 iterations; this was done on an all-in-one computer using only one 2.5GHz processor and 12GB RAM. The distance from the last turbine to the outlet was half the distance from the first turbine to the last turbine, or $\frac{1}{2}(max_x - min_x)$. Larger distances yielded the same results. It must be mentioned that it is not necessary to resolve the entire wake of the turbines until they recover the free stream value, this is possible thanks to the velocity outlet boundary condition which is *zeroGradient*. Figure 5.15 shows the power coefficients and the normalized power coefficients. The normalized coefficients were calculated by dividing all C_Ps by the maximum C_P. A coherent pattern is observed: the more the blockage, the lower the C_P value is. Also, the C_Ps of the turbines free of blockage were notably higher than those of the plot in Fig. 5.13, a maximum of 0.59 was found in one of the leading turbines, whereas a single isolated turbine had a C_P of 0.49. It is believed that the accelerated flow in some regions impacts the C_Ps, and thus different

values are obtained as if they were isolated.
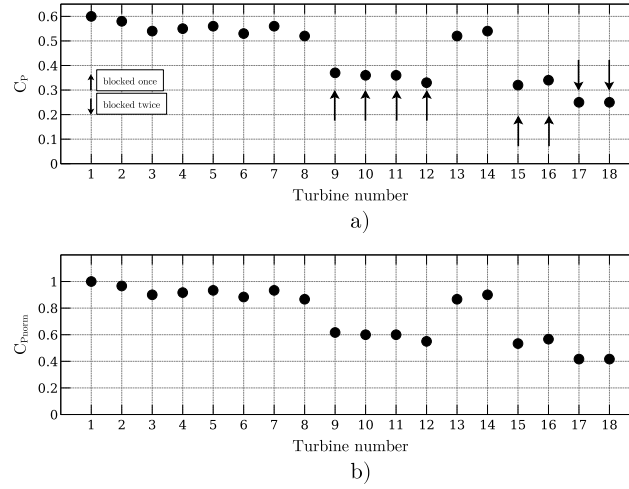
Figure 5.15: Wind farm array of 18 turbines using the 25 m-radius turbine from [1]. a) shows the current C_P and b) shows the normalized C_P. Arrows pointing upwards denote turbines that are blocked by only one turbine, whereas arrows that point downwards denote turbines that have been blocked by two turbines.

5.6 Discussion

The RANS-AC was successfully implemented in OpenFOAM. This was confirmed by the fact that it could achieve a power coefficient very similar to the stand-alone AC. Guidelines for selecting the mesh size and the thickness of the actuator were also given along with inlet boundary conditions for the RANS simulation. The model was validated against multi-turbine experiments and good agreement was found concerning the trend of the power coefficients in a row of four VAWTs. Unfortunately these multi-turbine experiments were done using small turbines which had a high solidity, this caused the model to wrongly predict the angles of attack, namely overestimating the angles of attack and thus getting the wrong coefficients of lift and tangential force. Thus results from the array of 18 turbines could not match the experimental data. An additional verification against a large VAWT LES simulation [1] with a low solidity was conducted to prove that the RANS-AC is indeed capable of model the wind farm power coefficients so long the leading turbines were not incorrectly predicted in the stall regime by the AC.

The comparison with the results of the wake of the large VAWT were in very good agreement. Although a multiple-turbine simulation was not done in [1], a simulation of an array of 18 turbines preserving the original relative distances between turbines in [10] was conducted. This time, the RANS-AC predicted a coherent pattern of the power coefficients across the array, e.g. the turbines free of blockage had higher power coefficients and the turbines that experienced more blockage from other turbines had lower power coefficients.

Chapter 6

Wind Farm Case Study

This last chapter will employ the RANS-AC in a fictitious wind farm. The purpose is to test two kinds of arrays; namely a staggered array and an array based on the fish-schooling idea proposed in [10]. Currently there no available results in the literature of VAWT farms nor there are studies about the influence of the wind direction and wind speed on the performance of the wind farm. It is hoped that the fish-school wind farm is able to be twice as dense while keeping a power coefficient close to the original staggered array. This would result in land cost savings and better rate of return.

6.1 Turbine verification with AC model

This section describes the geometrical and operational parameters of the turbine chosen for the wind farm layout study. One of the precautions that must be attended when using the AC model is to keep the turbine's solidity (σ) low. High values will cause the model to give inaccurate predictions. This is due to the fact that adding too many blades or having a large chord-to-radius ratio will introduce severe flow distortions which are not included in the model.

A large turbine from [4] with a low solidity and low chord-to-radius ratio was chosen for the study. This turbine will be used throughout the rest of the chapter. The characteristics of this turbine are described in Table 6.1.

Wind turbine characteristics					
$NACA$	N_B	R	c	Ω	σ
0018	3	10	0.432	33.4	0.065

Table 6.1: Current turbine used throughout this chapter. N_B is the number of blades, R is the radius, c is the chord and Ω is the rotational speed in rpm.

6.1.1 Sensitivity analysis

As said in the previous chapter, the RANS-AC model should be able to predict the power coefficient as close as the stand-alone AC. It is important to remind that the original AC is based on the Euler equations and no I value is needed as an input parameter, therefore the value of I at the inlet will be taken as 0.10 which is a typical value for offshore sites [32]. The computational domain is two-dimensional and comprises uniform squared cells; the distance from the center of the turbine to the inlet is 3D (rotor diameters) and so is the distance from

the center of the turbine to the sides of the domain. The distance from the turbine's center to the outlet boundary is 10D. Two meshes were made: a fine one which is based upon a 50×50 cells square surrounding the cylinder and a coarse one which is based upon a 30×30 cells square. The thickness of the actuator is subjective, a value of one chord was chosen for the fine mesh and a value of two chords was chosen for the coarse mesh. Figure 6.1 shows the comparison of the power coefficient (C_P) of the RANS-AC model with respect to the stand-alone AC. The tip-speed ratio is the quotient of the turbine's tangential velocity and the wind velocity.
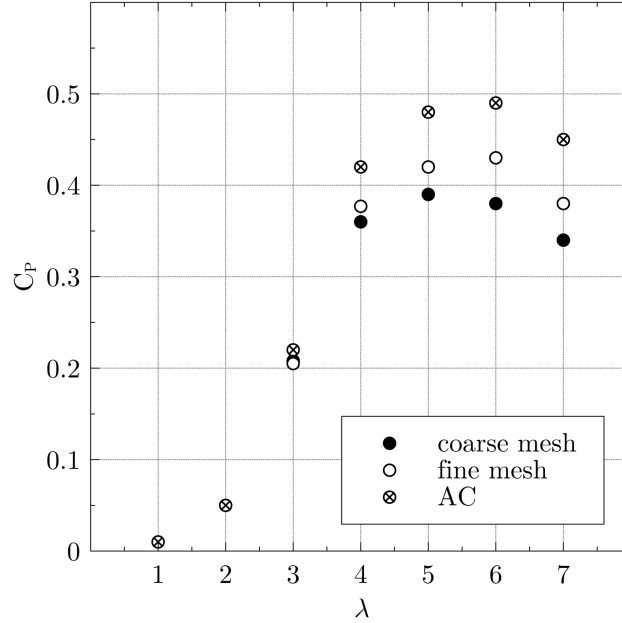
Figure 6.1: Power coefficients (AC vs RANS-AC) as a function of the tip-speed ratio λ.

It is believed that the discrepancy in Fig. 6.1 is due to the large distance between the front and rear parts of the actuator cylinder. The AC model assumes that the velocity inside the cylinder is constant streamwise whereas the RANS-AC actually takes into account viscous effects, therefore the velocity will decay streamwise before impacting the blades in the rear part of the rotor, hence the lower power coefficients exhibited by the RANS-AC. Without a validation with an existing turbine, it is hard to know which model yields the best results. The stand-alone AC will surely overestimate the power coefficient in the rear part of the rotor. Verifications and validations of the RANS-AC can be found in Martínez's paper [33].

6.2 Proposed wind farm arrays

In this section two different kinds of array configurations will be studied, namely a staggered array and an array based on the fish-schooling concept. According to [9], fish in shoals swim in such a way that each of them sheds counter-rotating vortices which help the shoal to minimize the energy needed for propulsion. It is not clear whether the wind farm is the right analogy to fish schools and little is know as to whether these counter-rotating vortices benefit the turbines in the back rows. The number of turbines is based on the staggered array, then the fish-school array will have twice as many turbines since every turbine in the staggered array will be replaced by a counter-rotating pair of turbines. The reason why the staggered array was chosen is because it is

less sensitive to the effect of wind direction provided it is aligned with the most frequent sector. Figures 6.2a and 6.2b show the two different arrays that will be studied throughout this work, notice that the flow is from left to right. The distance from one row to the next non-staggered row is 8 D; in Fig. 6.2b the distance between the axes of each pair is 1.5 D. Before moving on to the details of the simulations, a sensitivity analysis for the mesh size will be carried on. In order to save computational time, it is required to know how close the boundaries can be placed next to the turbines, e.g. placing them too close to the turbines could invalidate the boundary conditions, placing them too far apart could result in waste of computational time.

(a) Staggered array   (b) Fisch-school array
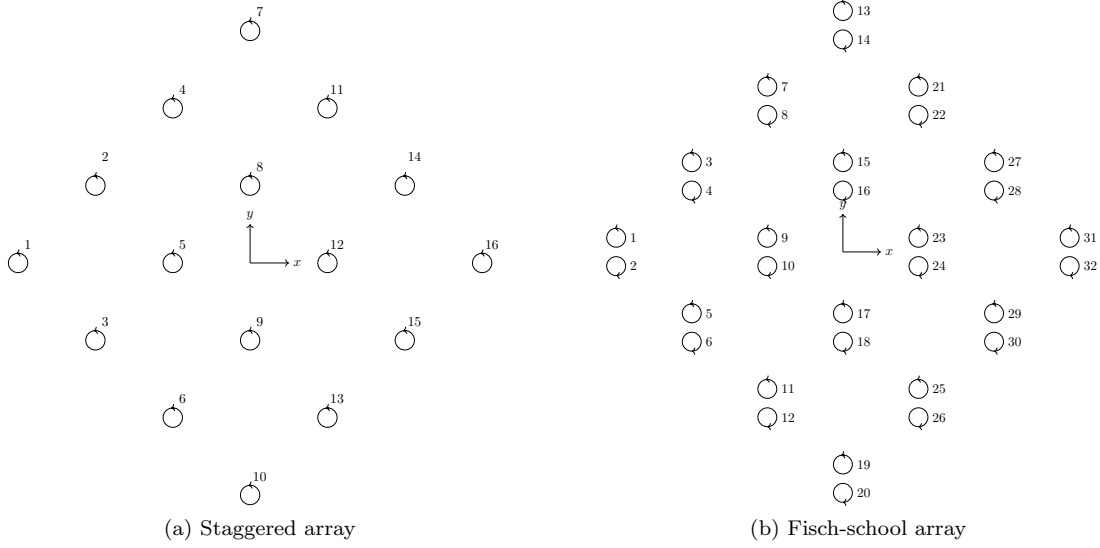
Figure 6.2: The two different arrays that will be used throughout this work.

6.2.1   Wind farm mesh sensitivity analysis

In order to save time during the simulations, four meshes are evaluated. The wind farm tested is that of Fig. 6.2a, the purpose is to choose the least computationally-expensive mesh without losing accuracy. Table 6.2 shows the characteristics of each mesh.

Tested meshes				
	square-coarse	rectangular-coarse	square-fine	rectangular-fine
enclosing square size in cells	30×30	30×30	50×50	50×50
min_x	$t_{min_x} - 6R$	$t_{min_x} - 6R$	$t_{min_x} - 6R$	$t_{min_x} - 6R$
max_x	$t_{max_x} + 6R$	$t_{max_x} + 12R$	$t_{max_x} + 6R$	$t_{max_x} + 12R$
min_y	$t_{min_y} - 6R$	$t_{min_y} - 6R$	$t_{min_y} - 6R$	$t_{min_y} - 6R$
max_y	$t_{max_y} + 6R$	$t_{max_y} + 6R$	$t_{max_y} + 6R$	$t_{max_y} + 6R$
thickness	$2c$	$2c$	c	c

Table 6.2: Four kinds of meshes used for the sensitivity study of a wind farm. $\lambda = 4$, $U_\infty = 8.74 \text{ m s}^{-1}$. t is the position of a turbine, e.g. t_{min_x} is the leftmost turbine's position.

Figure 6.3 shows the power coefficients for each mesh. Fine meshes exhibit a slightly larger

power coefficient. The back rows are the ones exhibiting more discrepancy but overall the trend is the same. Figure 6.4 shows the error between the smallest coarse mesh and the largest fine mesh. The error is about 8% in the turbines that have been blocked by two or more turbines, this is acceptable since the C_P of turbine 16 of the smallest coarse mesh is 0.134 and the C_P of the larges fine mesh is 0.147, compared to the leading turbine's average C_P (coarse and fine mesh) which is about 0.366, their respective normalized C_P is 0.366 and 0.401.

(a) Rectangular mesh

(b) Square mesh
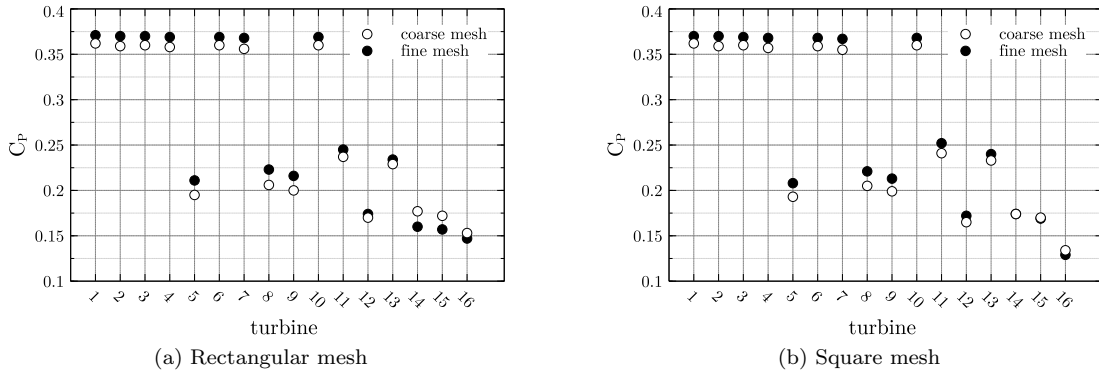
Figure 6.3: Two different meshes used for sensitivity analysis.
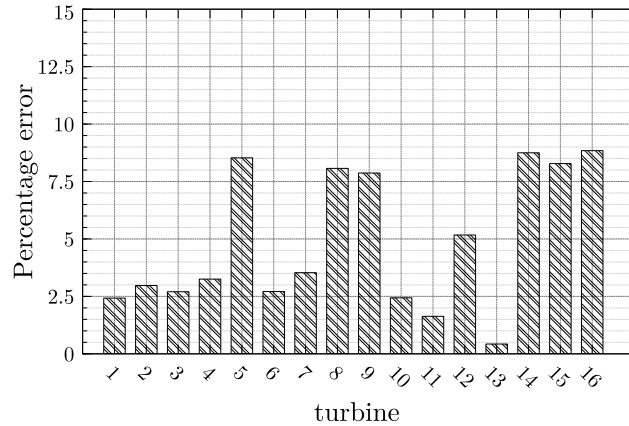
Figure 6.4: Smallest coarse mesh versus largest fine mesh power coefficient error.

6.2.2 Influence of wind direction and wind speed

Figure 6.2a shows that the wind farm array is symmetrical with respect to the y axis, this means that it is not necessary to study the full 360° sector but only half of it. Figure 6.5 shows the nine directions taken into account in this study. Only the most critical wind directions are taken into account. Four different speeds are chosen: 6, 8, 10 and 12 m s^{-1}. The reason being is that most wind turbines begin to operate at 5 m s^{-1}, also wind speeds higher than 12 m s^{-1} are rare during the whole year. These considerations will also be applied to the fish-school array. Results in tabular form can be found in Appendix D.
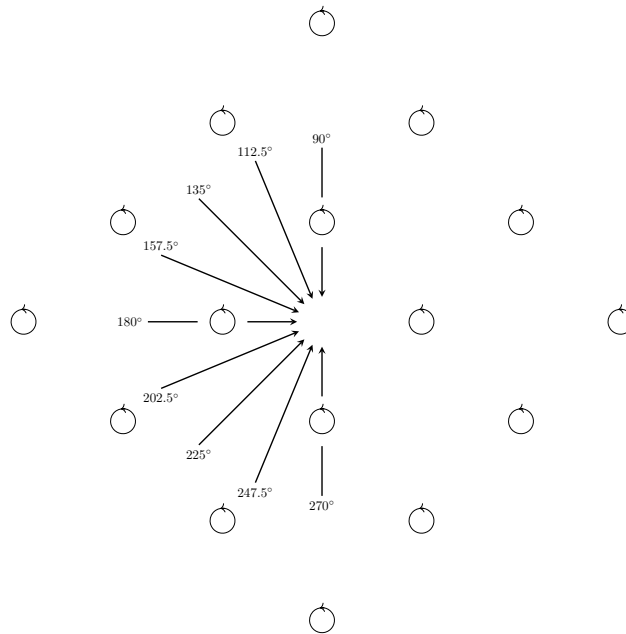
Figure 6.5: Wind directions that will be used in the current study. Only half the entire sector will be used due to symmetry.

Turbulence intensity values depends strongly on atmospheric conditions, wind speed and as well as the roughness of the terrain. A site located in Bockstigen, Sweden will be taken as a reference in order to obtain free stream values of I at different wind speeds. The site is located offshore and data is provided in [32]. Since the data is a scatter plot from measured values at different speeds, the values in between the minimum and maximum record were chosen from the plot. Table 6.3 shows the minimum, mean and maximum values of I for different wind speeds. The height of the mast is 40 m.

Turbulence intensity according to wind speed					
ms^{-1}	6	8	10	12	14
min	0.07	0.07	0.075	0.08	0.07
max	0.25	0.15	0.125	0.12	0.09
mean	0.16	0.11	0.100	0.10	0.08

Table 6.3: Wind data at 40 m from Bockstigen, Gotland, Sweden.

Figure 6.6 shows the average power coefficient of the entire farm as a function of the wind direction and wind speed. The fish-schooling array shows detrimental results when the wind blows from the north or the south since half the turbines are blocked by their twins. On the other hand, the fish-schooling array shows an increase of 16% when the wind blows from the west ($180°$) for the case of 8 m s^{-1}, an increase of 10% is seen for the case of 10 m s^{-1} with wind blowing from the west. This increase in the power coefficient is more or less in accordance to [4], which is 15% roughly for a pair of turbines. Interestingly, at 12 m s^{-1} the average C_P of the farm almost reaches the value of 0.20, which is the C_P of an isolated turbine when $\lambda = 4$, see Fig. 6.1.
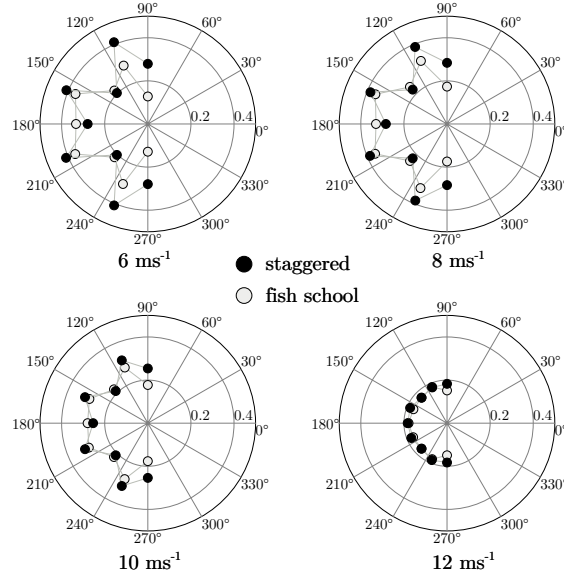
Figure 6.6: Average power coefficient as a function of direction and wind speed.

Power density is the quotient of the total power produced by the farm divided by the area of land occupied by the turbine; in other words it is the power extracted by square meter. The surface area of the farm was taken from Fig. 6.2a, the distance from turbine 1 to turbine 16 is 480 m, therefore the surface area is 115200 m^2. In order to calculate the power of a single turbine, it is necessary to know the swept area S which will be taken as $(2R)(2R)$, since $2R$ is the diameter of the turbine. The height of the turbine will be taken as the diameter of the turbine. Equation 6.1 is necessary to calculate the power of a turbine.

$$P = \frac{1}{2}\rho V_\infty^3 S C_P \qquad\qquad\qquad\qquad\qquad\qquad\qquad\qquad\qquad (6.1)$$

The V_∞ term will be based on the free stream speed for each turbine. Figure 6.7 shows the power density of the farm as a function of direction and wind speed, this was calculated as the sum of all of the turbines' power divided by the surface area of the farm. The results show an twofold increase in power density in almost all directions for a fish-schooling array, the only cases where no increase is seen is in the case of 6 m s^{-1} when the wind blows from the north and the south. The almost-twofold increase is expected since there are twice as many turbines in the fish-school farm. There seems to be a dilemma in choosing fish-schooling farms; on the one hand compactness can yield twice as much power, on the other hand, these fish-schooling arrays are not necessarily more efficient (Fig. 6.6 shows that the fish-schooling farm is only more efficient than the conventional farms in 3 out of the 9 directions).
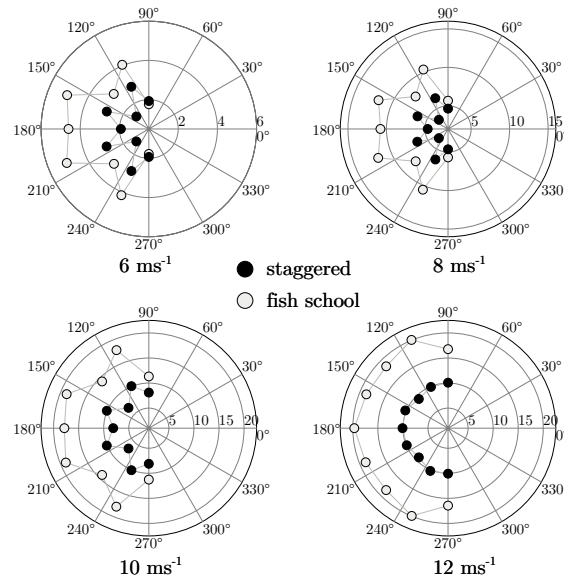
Figure 6.7: Wind farm power density $\mathrm{W\,m^{-2}}$ as a function of direction and wind speed.

According to [34] HAWT farms produce around 2–3 $\mathrm{W\,m^{-2}}$. Table 6.4 shows the fish-school and conventional farm average power density (from all directions) for each wind speed. Notice that in actuality the wind does not blow with the same probability from all directions, therefore, cases in which half the turbines are blocked in the fish-school array (north and south) must be avoided by placing the turbines strategically. The fact of getting almost twice as much power density from the same occupied land can reduce costs dramatically since cabling costs and land rental would probably be half the original cost.

Average power density $\mathrm{W\,m^{-2}}$			
$\mathrm{m\,s^{-1}}$	fish-school	conventional	improvement ratio
6	3.8	2.2	1.72
8	9.6	5.2	1.85
10	16.4	8.7	1.88
12	18.8	9.9	1.9

Table 6.4: Average power density from all directions.

6.3   Discussion

The RANS actuator cylinder was used to assess the performance of two different wind turbine arrays, namely a staggered array and another staggered array using pairs of counter-rotating turbines. The power coefficient of a single isolated turbine was tested against the stand-alone AC and the results were satisfactory except at high tip-speed ratios where the velocity of the wind speed is low. This does not suggest that the RANS-AC is wrong but its C_P at low wind speeds simply differed from the stand-alone AC because the RANS-AC does indeed take into

account viscous effects, therefore the wind speed impacting the rear part of the rotor is lower than that of the stand-alone AC due to the large distance (20 m maximum, which is the turbine's diameter) from the upwind part of the rotor to the downwind part of the rotor.

A mesh sensitivity analysis was carried on for a wind farm in order to use the less time-consuming mesh without sacrificing accuracy. The study was undertaken and several simulations at different wind speeds and directions were done. A coarse mesh was found to be optimal. The value of turbulence intensity at the inlet was chosen based on data acquired from an offshore site off the coast of Sweden.

The staggered array outperformed the fish-school array in most directions but the fish-school array yielded higher global power coefficients when the wind blows from the west (the case in which all pairs are facing the wind). Improvements up to 16% percent were seen depending on the wind speed. By contrast, the fish-school array outperformed the staggered array by a factor of two in terms of power density. Given the fact that typical HAWT farms yield around 2–3 $W\,m^{-2}$, it can be said that VAWT farms yield in this case 5 or 3 times more power density when the wind blows at 8 $W\,m^{-2}$. The fish-school array power density averaged over all directions was practically twice as high as in the staggered array, this proves that the fish-school array may be able to extract twice as much energy so long it is placed strategically. VAWT farms could be compacted within a surface area half the original size and still get almost twice as much power density. This could reduce land costs as well as cabling significantly.

Conclusions

The mayor contribution of this work was the implementation of a virtual vertical-axis wind turbine, that is, a modified steady, incompressible and turbulent solver that uses the actuator-cylinder model as a surrogate for calculating the volumetric forces that the turbine exerts on the fluid. This is crucial since the computational cost is greatly reduced since there are no blades in the domain, which would need an extremely fine mesh. The mesh is now uniform across the domain and the wake of a single turbine can be resolved in a few seconds depending the size of the domain. Moreover, several turbines can be placed across the domain and each one of the wakes takes into account the influence of the other wakes automatically. Up to this day, only simple models were available for the computation of vertical-axis wind turbine farms; more complicated models were also available but the computational cost was out of the scope of a personal computer.

The model depends strongly on the solidity of the turbine, so turbines with many blades or a large chord-to-radius ratio must be avoided or else the results are not guaranteed, this is due to the actuator-cylinder model's limitations. Boundary conditions must take into account the inlet turbulence intensity, therefore the precise value will affect the shapes of the wakes.

The model was tested against experimental data, coherent patterns were observed as for the power coefficient of each turbine. A verification against a wake from numerical simulations was done and the results were satisfactory.

Finally, the model was used to compare two different kinds of arrays: a staggered array and a fish-school array. The staggered array proved to be more efficient since it is more sparse and thus less blocking effects are present; on the other hand, the fish-school array achieved more power density and was only more efficient when the pairs of turbines were facing the wind directly. With a good collocation strategy, the fish-school array can occupy half the land and yet achieve a twofold increase in power density.

It is hoped that these results are considered by large energy companies installing vertical-axis wind turbines in the future.

Appendix A

Derivation of the Equations for the Perturbation Velocities

The linear part of equations 4.15 and 4.16 is:

$$w_x = -p(f) + \int_{-\infty}^{x} f_x \cdot dx' \tag{A.1}$$

$$w_y = -\int_{-\infty}^{x} \frac{\partial}{\partial y} p(f) dx' + \int_{-\infty}^{x} f_y \cdot dx' \tag{A.2}$$

Equation 4.13 contains the volume forces in the x and y directions:

$$p(f) = \frac{1}{2\pi} \int \int \frac{f_x(x-\xi) + f_y(y-\eta)}{(x-\xi)^2 + (y-\eta)^2} d\xi d\eta \tag{A.3}$$

The simple actuator cylinder model only considers the normal volume forces f_n, so, f_x and f_y only depend on f_n. The actuator cylinder model modification by Cheng [20] includes the tangential volume forces f_t, therefore, the projections in the x and y directions will contain extra terms:

$$f_x = -f_n \sin\theta - f_t \cos\theta \tag{A.4}$$

$$f_y = f_n \cos\theta - f_t \sin\theta \tag{A.5}$$

The normal and tangential loads are defined as following:

$$Q_n(\theta) = \lim_{\epsilon \to 0} \int_{R-\epsilon}^{R+\epsilon} f_n(\theta) \cdot dr \tag{A.6}$$

$$Q_t(\theta) = \lim_{\epsilon \to 0} \int_{R-\epsilon}^{R+\epsilon} f_t(\theta) \cdot dr \tag{A.7}$$

Substituting f_x and f_y in equation A.3 and using polar coordinates instead of dummy variables yields:

$$
\begin{aligned}
p(f) = &\frac{1}{2\pi} \int_0^{2\pi} Q_n(\theta) \frac{-(x+\sin(\theta))\sin(\theta) + (y-\cos(\theta))\cos(\theta)}{(x+\sin(\theta))^2 + (y-\cos(\theta))^2} d\theta \\
&+ \frac{1}{2\pi} \int_0^{2\pi} Q_t(\theta) \frac{-(x+\sin(\theta))\cos(\theta) - (y-\cos(\theta))\sin(\theta)}{(x+\sin(\theta))^2 + (y-\cos(\theta))^2} d\theta
\end{aligned}
\tag{A.8}
$$

In order to obtain the first term in equation A.2, it is necessary to derivate the previous equation with respect to y and integrate it with respect to x. The outcome is:

$$\int_{-\infty}^{x} \frac{\partial p(f)}{\partial y} dx' = -\frac{1}{2\pi} \int_{0}^{2\pi} Q_n(\theta) \frac{-(x+\sin(\theta))\cos(\theta) - (y-\cos(\theta))\sin(\theta)}{(x+\sin(\theta))^2 + (y-\cos(\theta))^2} d\theta$$
$$+ \frac{1}{2\pi} \int_{0}^{2\pi} Q_t(\theta) \frac{-(x+\sin(\theta))\sin(\theta) + (y-\cos(\theta))\cos(\theta)}{(x+\sin(\theta))^2 + (y-\cos(\theta))^2} d\theta \tag{A.9}$$

The last term to work out is the integration of the volume force in the x direction:

$$\int_{-\infty}^{x} f_x \cdot dx' \tag{A.10}$$

Care must be taken when evaluating this integral. For the inner part of the cylinder, the integration of the volume force becomes:

$$\int_{-\infty}^{x} f_x \cdot dx' = \int_{-\infty}^{0} f_x \cdot dx' \tag{A.11}$$

The x' is a dummy variable for the x coordinate, while a plain x represents the horizontal coordinate of the evaluation point. From simple trigonometry the following is obtained:

$$x' = -\sqrt{r^2 - y^2} \tag{A.12}$$

$$dx' = -\frac{r}{\sqrt{r^2 - y^2}} dr \tag{A.13}$$

The volume force in the horizontal direction becomes:

$$f_x = -f_n \sin\theta - f_t \cos\theta = -f_n \frac{\sqrt{r^2 - y^2}}{r} - f_t \frac{y}{r} \tag{A.14}$$

Equation A.10 is now:

$$\int_{-\infty}^{x} f_x \cdot dx' = \lim_{\epsilon \to 0} \int_{R+\epsilon}^{R-\epsilon} \left(-f_n \frac{\sqrt{r^2 - y^2}}{r} - f_t \frac{y}{r} \right) \left(-\frac{r}{\sqrt{r^2 - y^2}} \right) dr$$
$$= -\lim_{\epsilon \to 0} \int_{R-\epsilon}^{R+\epsilon} \left(f_n + f_t \frac{y}{\sqrt{r^2 - y^2}} \right) dr \tag{A.15}$$
$$= -Q_n(\arccos y) - Q_t(\arccos y) \frac{y}{\sqrt{1 - y^2}}$$

For the leeward part of the cylinder, the integration of the volume force is given by:

$$\int_{-\infty}^{x} f_x \cdot dx' = \int_{-\infty}^{0} f_x \cdot dx' + \int_{0}^{x} f_x \cdot dx' \tag{A.16}$$

The first term has already been computed, but the procedure for the second term is similar to that of the first term:

$$x' = \sqrt{r^2 - y^2} \tag{A.17}$$

$$dx' = \frac{r}{\sqrt{r^2 - y^2}} dr \tag{A.18}$$

It is important to bear in mind that x is negative the the windward part and positive in the leeward part, thus, the sines for x will also have different signs in the windward and leeward part.

$$f_x = -f_n \sin\theta - f_t \cos\theta = f_n \frac{\sqrt{r^2 - y^2}}{r} - f_t \frac{y}{r} \tag{A.19}$$

$$\int_0^x f_x \cdot dx' = \lim_{\epsilon \to 0} \int_{R-\epsilon}^{R+\epsilon} \left(f_n \frac{\sqrt{r^2 - y^2}}{r} - f_t \frac{y}{r} \right) \left(\frac{r}{\sqrt{r^2 - y^2}} \right) dr$$

$$= -\lim_{\epsilon \to 0} \int_{R-\epsilon}^{R+\epsilon} \left(f_n - f_t \frac{y}{\sqrt{r^2 - y^2}} \right) dr \tag{A.20}$$

$$= Q_n(-\arccos y) - Q_t(-\arccos y) \frac{y}{\sqrt{1-y^2}}$$

Having all the terms worked out in equations A.1 and A.2, the induced velocities have the following final form:

$$w_x = -\frac{1}{2\pi} \int_0^{2\pi} Q_n(\theta) \frac{-(x+\sin(\theta))\sin(\theta) + (y-\cos(\theta))\cos(\theta)}{(x+\sin(\theta))^2 + (y-\cos(\theta))^2} d\theta$$

$$-\frac{1}{2\pi} \int_0^{2\pi} Q_t(\theta) \frac{-(x+\sin(\theta))\cos(\theta) - (y-\cos(\theta))\sin(\theta)}{(x+\sin(\theta))^2 + (y-\cos(\theta))^2} d\theta$$

$$- Q_n(\arccos y)^* + Q_n(-\arccos y)^{**} \tag{A.21}$$

$$- \left(Q_t(\arccos y) \frac{y}{\sqrt{1-y^2}} \right)^* - \left(Q_t(-\arccos y) \frac{y}{\sqrt{1-y^2}} \right)^{**}$$

$$w_y = -\frac{1}{2\pi} \int_0^{2\pi} Q_n(\theta) \frac{-(x+\sin(\theta))\cos(\theta) - (y-\cos(\theta))\sin(\theta)}{(x+\sin(\theta))^2 + (y-\cos(\theta))^2} d\theta$$

$$+\frac{1}{2\pi} \int_0^{2\pi} Q_t(\theta) \frac{-(x+\sin(\theta))\sin(\theta) + (y-\cos(\theta))\cos(\theta)}{(x+\sin(\theta))^2 + (y-\cos(\theta))^2} d\theta \tag{A.22}$$

Appendix B

Modification of the Linear Solution

This section shows details about the derivation of the thrust coeffcient, induction factor and correction factor for the perturbation velocities.
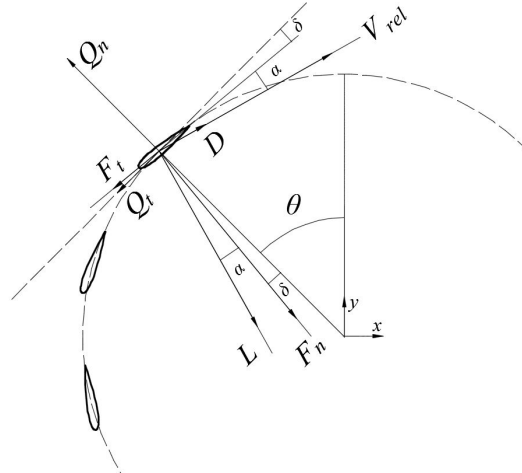
Figure B.1: *Streamwise projection of normal and tangential forces.*

From Figure 4.4 the thrust force is obtained by means of projecting the normal and tangential forces onto the direction of the free stream –horizontally.

$$F_x(\theta) = F_n(\theta)\sin(\theta - \delta) - F_t(\theta)\cos(\theta - \delta) \tag{B.1}$$

The average torque per unit meter in one revolution is:

$$T = \frac{1}{2\pi} N_B \int_0^{2\pi} F_x(\theta)d\theta \tag{B.2}$$

The non-dimensional thrust, otherwise known as the thrust coefficient, is defined in the following manner:

$$C_T = \frac{T}{\frac{1}{2}\rho V_\infty^2 2R} \tag{B.3}$$

Notice carefully that $2R$ is the frontal area per unit length. Substituting equations B.1 and B.2 in the previous equation yields the following:

$$C_T = \frac{N_B}{2\pi\rho V_\infty^2 R} \int_0^{2\pi} (F_n(\theta)\sin(\theta - \delta) - F_t(\theta)\cos(\theta - \delta))\, d\theta \tag{B.4}$$

$$C_T = \frac{N_B}{2\pi\rho V_\infty^2 R} \int_0^{2\pi} [(F_n(\theta)\cos\delta - F_t(\theta)\sin\delta))\sin\theta - (F_n(\theta)\sin\delta + F_t(\theta)\cos\delta))\cos\theta]\, d\theta \tag{B.5}$$

From equations 4.42 and 4.43 the C_T can be expressed in terms of the non-dimensional normal and tangential loads:

$$C_T = \int_0^{2\pi} (Q_n(\theta)\sin\theta + Q_t(\theta)\cos\theta)\, d\theta \tag{B.6}$$

The modification of the linear solution by Madsen [21] is achieved by multiplying the perturbation velocities by a correction factor:

$$w_{x,mod} = k_a \cdot w_x \tag{B.7}$$

$$w_{y,mod} = k_a \cdot w_y \tag{B.8}$$

In which k_a is given by:

$$k_a = \frac{1}{1-a} \tag{B.9}$$

Where a is the global induction factor defined by the momentum theory:

$$C_t = 4a(1-a) \tag{B.10}$$

The previous equation is only valid for $a < 0.333$. The linear solution of the thrust coefficient according to Madsen [21] is $C_T = 4a_{lin}$. It can be easily seen that the correction factor is nothing but the ratio of the thrust coefficients from the linear solution and the momentum theory. The induction factor can be determined in terms of the thrust coefficient from another article provided by Larsen and Madsen [20]:

$$a = k_3 C_T^3 + k_2 C_T^2 + k_1 C_T + k_0 \tag{B.11}$$

Where C_T is given by equation B.6.

Appendix C

Derivation of the power coefficient

Raw mechanical power of one blade can be obtained from the next equation:

$$P(\theta) = \omega T(\theta) \tag{C.1}$$

From Figure 4.3 it is observed that torque originates from the net tangential force times the radius of the turbine:

$$T(\theta) = F_r(\theta)R = (F_t(\theta)\cos\delta + F_n(\theta)\sin\delta)R \tag{C.2}$$

Where δ is the blade's pitch angle. The average power is calculated by integrating the local mechanical power, multiplying it by the N_B blades and averaging it by 2π, which stands for one revolution.

$$P_{mean} = \frac{1}{2\pi} \int_0^{2\pi} \omega N_B T(\theta) d\theta \tag{C.3}$$

By definition, the power coefficient per unit length of the rotor is given by:

$$C_P = \frac{P_{mean}}{\frac{1}{2}\rho V_\infty^3 2R} \tag{C.4}$$

By substituting C.3 into C.4 the following is obtained:

$$C_P = \frac{\omega R}{V_\infty} \int_0^{2\pi} \frac{N_B \left(F_t(\theta)\cos\delta + F_n(\theta)\sin\delta\right)}{2\pi R \rho V_\infty^2} d\theta \tag{C.5}$$

Notice that the term before the integral is nothing but the tip-speed ratio of the turbine. The integrand is the negative of the nondimensional tangential load of the actuator disk. Having said that, the power coefficient can be simplified to:

$$C_P = -\lambda \int_0^{2\pi} Q_t(\theta) d\theta \tag{C.6}$$

The previous equations hold for the case of counter-clockwise rotation. For clockwise rotation, the minus sign is ommitted in equation C.6. The derivation procedure is ommitted here but it can be performed in the same way.

Appendix D

Power coefficients of the arrays

	6	6	6	6	6	6	6	6	6
	90	112.5	135	157.5	180	202.5	225	247.5	270
t01	0.406681	0.394516	0.441751	0.444282	0.409509	0.442702	0.443196	0.385107	0.39896
t02	0.406125	0.414871	0.457335	0.424656	0.404835	0.444855	0.16121	0.457078	0.234033
t03	0.232478	0.459019	0.156636	0.44858	0.406729	0.424684	0.455514	0.410583	0.401525
t04	0.406729	0.424684	0.455514	0.410583	0.401525	0.451868	0.144225	0.275776	0.160517
t05	0.190913	0.492476	0.146349	0.479022	0.183457	0.484918	0.149533	0.48763	0.193066
t06	0.160606	0.28025	0.139947	0.452628	0.406125	0.414871	0.457335	0.424656	0.404835
t07	0.409509	0.442702	0.443196	0.385107	0.39896	0.467485	0.102809	0.263462	0.114427
t08	0.183457	0.484918	0.149533	0.48763	0.193066	0.504744	0.101738	0.364116	0.163497
t09	0.163497	0.370299	0.100335	0.508617	0.190913	0.492476	0.146349	0.479022	0.183457
t10	0.114427	0.270862	0.101009	0.472117	0.406681	0.394516	0.441751	0.444282	0.409509
t11	0.404835	0.444855	0.16121	0.457078	0.234033	0.319094	0.0742083	0.346385	0.160606
t12	0.193066	0.504744	0.101738	0.364116	0.163497	0.370299	0.100335	0.508617	0.190913
t13	0.160517	0.34684	0.0729903	0.32411	0.232478	0.459019	0.156636	0.44858	0.406729
t14	0.401525	0.451868	0.144225	0.275776	0.160517	0.34684	0.0729903	0.32411	0.232478
t15	0.234033	0.319094	0.0742083	0.346385	0.160606	0.28025	0.139947	0.452628	0.406125
t16	0.39896	0.467485	0.102809	0.263462	0.114427	0.270862	0.101009	0.472117	0.406681
avg	**0.2792**	**0.4106**	**0.203**	**0.409**	**0.2792**	**0.4106**	**0.203**	**0.409**	**0.2792**

Figure D.1: Staggered array at 6 m s^{-1}

	8	8	8	8	8	8	8	8	8
	90	112.5	135	157.5	180	202.5	225	247.5	270
t01	0.384596	0.378168	0.40444	0.404374	0.387335	0.405079	0.404889	0.371302	0.379955
t02	0.384367	0.388955	0.411745	0.394708	0.384134	0.407675	0.206405	0.413587	0.25427
t03	0.250311	0.412091	0.198777	0.409796	0.385033	0.394507	0.412141	0.386618	0.381793
t04	0.385033	0.394507	0.412141	0.386618	0.381793	0.411064	0.179355	0.284452	0.189567
t05	0.217008	0.432609	0.195705	0.426711	0.20935	0.430467	0.199775	0.429235	0.220507
t06	0.187054	0.292185	0.168645	0.408758	0.384367	0.388955	0.411745	0.394708	0.384134
t07	0.387335	0.405079	0.404889	0.371302	0.379955	0.417333	0.163121	0.293364	0.143256
t08	0.20935	0.430467	0.199775	0.429235	0.220507	0.440445	0.136413	0.36088	0.181618
t09	0.181618	0.366882	0.132984	0.440651	0.217008	0.432609	0.195705	0.426711	0.20935
t10	0.143256	0.304257	0.155343	0.418007	0.384596	0.378168	0.40444	0.404374	0.387335
t11	0.384134	0.407675	0.206405	0.413587	0.25427	0.336467	0.119513	0.368407	0.187054
t12	0.220507	0.440445	0.136413	0.36088	0.181618	0.366882	0.132984	0.440651	0.217008
t13	0.189567	0.369408	0.116835	0.343487	0.250311	0.412091	0.198777	0.409796	0.385033
t14	0.381793	0.411064	0.179355	0.284452	0.189567	0.369408	0.116835	0.343487	0.250311
t15	0.25427	0.336467	0.119513	0.368407	0.187054	0.292185	0.168645	0.408758	0.384367
t16	0.379955	0.417333	0.163121	0.293364	0.143256	0.304257	0.155343	0.418007	0.384596
avg	**0.2838**	**0.3867**	**0.2254**	**0.3846**	**0.2838**	**0.3867**	**0.2254**	**0.3846**	**0.2838**

Figure D.2: Staggered array at 8 m s^{-1}

	10	10	10	10	10	10	10	10	10
	90	112.5	135	157.5	180	202.5	225	247.5	270
t01	0.319132	0.318979	0.32275	0.319006	0.31854	0.322746	0.318783	0.310418	0.314055
t02	0.319119	0.320551	0.321959	0.317178	0.316258	0.322571	0.218043	0.323759	0.242196
t03	0.23883	0.319929	0.210911	0.326655	0.318719	0.3175	0.325298	0.319494	0.315057
t04	0.318719	0.3175	0.325298	0.319494	0.315057	0.322974	0.181439	0.275704	0.187275
t05	0.219422	0.329721	0.2148	0.32877	0.214738	0.330853	0.219246	0.324683	0.223121
t06	0.182479	0.281177	0.167645	0.31927	0.319119	0.320551	0.321959	0.317178	0.316258
t07	0.31854	0.322746	0.318783	0.310418	0.314055	0.32273	0.162534	0.287184	0.154758
t08	0.214738	0.330853	0.219246	0.324683	0.223121	0.32473	0.153322	0.314067	0.177738
t09	0.177738	0.299661	0.148567	0.333068	0.219422	0.329721	0.2148	0.32877	0.214738
t10	0.154758	0.291746	0.150741	0.324698	0.319132	0.318979	0.32275	0.319006	0.31854
t11	0.316258	0.322571	0.218043	0.323759	0.242196	0.310207	0.130342	0.315111	0.182479
t12	0.223121	0.32473	0.153322	0.314067	0.177738	0.299661	0.148567	0.333068	0.219422
t13	0.187275	0.312304	0.127002	0.308648	0.23883	0.319929	0.210911	0.326655	0.318719
t14	0.315057	0.322974	0.181439	0.275704	0.187275	0.312304	0.127002	0.308648	0.23883
t15	0.242196	0.310207	0.130342	0.315111	0.182479	0.281177	0.167645	0.31927	0.319119
t16	0.314055	0.32273	0.162534	0.287184	0.154758	0.291746	0.150741	0.324698	0.319132
avg	**0.2538**	**0.3155**	**0.2108**	**0.3155**	**0.2538**	**0.3155**	**0.2108**	**0.3155**	**0.2538**

Figure D.3: Staggered array at 10 m s^{-1}

	12	12	12	12	12	12	12	12	12
	90	112.5	135	157.5	180	202.5	225	247.5	270
t01	0.18454	0.186638	0.183444	0.178095	0.186692	0.184306	0.177541	0.184764	0.185515
t02	0.185469	0.186309	0.176611	0.180838	0.185974	0.180684	0.17546	0.179337	0.178185
t03	0.205699	0.176009	0.198586	0.183375	0.186746	0.181537	0.183943	0.184207	0.185688
t04	0.186746	0.181537	0.183943	0.184207	0.185688	0.179412	0.160729	0.207231	0.171512
t05	0.197589	0.177872	0.188318	0.181811	0.189576	0.174747	0.188651	0.175405	0.181756
t06	0.1732	0.175545	0.162484	0.176682	0.185469	0.186309	0.176611	0.180838	0.185974
t07	0.186692	0.184306	0.177541	0.184764	0.185515	0.180531	0.152444	0.200792	0.153465
t08	0.189576	0.174747	0.188651	0.175405	0.181756	0.173117	0.161377	0.197633	0.169407
t09	0.169407	0.16895	0.157037	0.181654	0.197589	0.177872	0.188318	0.181811	0.189576
t10	0.153465	0.175606	0.142766	0.181962	0.18454	0.186638	0.183444	0.178095	0.186692
t11	0.185974	0.180684	0.17546	0.179337	0.178185	0.192279	0.136288	0.186647	0.1732
t12	0.181756	0.173117	0.161377	0.197633	0.169407	0.16895	0.157037	0.181654	0.197589
t13	0.171512	0.178764	0.132206	0.185251	0.205699	0.176009	0.198586	0.183375	0.186746
t14	0.185688	0.179412	0.160729	0.207231	0.171512	0.178764	0.132206	0.185251	0.205699
t15	0.178185	0.192279	0.136288	0.186647	0.1732	0.175545	0.162484	0.176682	0.185469
t16	0.185515	0.180531	0.152444	0.200792	0.153465	0.175606	0.142766	0.181962	0.18454
avg	**0.1826**	**0.1795**	**0.1674**	**0.1854**	**0.1826**	**0.1795**	**0.1674**	**0.1854**	**0.1826**

Figure D.4: Staggered array at 12 m s^{-1}

	6	6	6	6	6	6	6	6	6
	90	112.5	135	157.5	180	202.5	225	247.5	270
t01	0.368997	0.384884	0.426745	0.462522	0.444595	0.480557	0.488093	0.148198	0.0890983
t02	0.102116	0.13831	0.497865	0.488809	0.453286	0.467222	0.426867	0.377132	0.361299
t03	0.365247	0.373711	0.443925	0.439042	0.433782	0.52445	0.0994872	0.184359	0.0493123
t04	0.0723146	0.213697	0.548025	0.491289	0.470638	0.209839	0.259181	0.472641	0.164266
t05	0.176523	0.47316	0.277785	0.196257	0.468476	0.489442	0.538879	0.232343	0.0641999
t06	0.0584799	0.174542	0.105868	0.539689	0.446907	0.447442	0.446405	0.366291	0.36073
t07	0.365063	0.386542	0.444177	0.426542	0.444573	0.487682	0.0362533	0.0554748	-0.000936119
t08	0.0580875	0.261108	0.551175	0.445109	0.458609	0.131028	0.346993	0.258454	0.0711921
t09	0.108123	0.506945	0.174593	0.370634	0.247487	0.562259	0.175167	0.285269	0.0205771
t10	0.0248615	0.270085	0.183746	0.574536	0.255753	0.39154	0.173239	0.506024	0.103276
t11	0.0751363	0.271406	0.368488	0.12566	0.461606	0.445211	0.544935	0.28509	0.0539305
t12	0.00307543	0.0528311	0.0454831	0.503249	0.461252	0.433621	0.45258	0.389142	0.36355
t13	0.357379	0.409754	0.426566	0.428989	0.476025	0.461861	0.00163704	0.027303	-0.0356191
t14	0.0481379	0.312876	0.535042	0.447359	0.473449	0.0665282	0.321742	0.153841	0.0274645
t15	0.101887	0.516157	0.180261	0.49905	0.278162	0.48085	-0.00400296	0.203257	0.00567296
t16	0.0206846	0.375951	0.193745	0.57239	0.279092	0.270085	0.0749288	0.191921	0.0835121
t17	0.0823886	0.184928	0.0832019	0.252673	0.286841	0.566661	0.196309	0.399586	0.0202453
t18	0.00607331	0.185415	-0.00268038	0.498049	0.291749	0.513087	0.187214	0.519051	0.103151
t19	0.0265802	0.159334	0.343261	0.0677253	0.481158	0.452292	0.531039	0.334889	0.0482498
t20	-0.035308	0.0229696	0.00877436	0.466792	0.495539	0.442034	0.435598	0.414148	0.360457
t21	0.360479	0.442737	0.114188	0.498398	0.249637	0.337232	-0.0480726	0.118337	0.000888159
t22	0.0548456	0.367767	0.34065	0.4007	0.418403	0.127448	0.0359488	0.214766	0.0789006
t23	0.105948	0.500184	0.000123227	0.280698	0.165538	0.328294	0.0855875	0.478012	0.0226487
t24	0.0192235	0.451711	0.0783916	0.333758	0.166904	0.29103	-0.000109184	0.516714	0.113345
t25	0.072782	0.211294	0.0444663	0.124185	0.427317	0.38699	0.356695	0.389007	0.0591877
t26	-0.00237412	0.108663	-0.0477108	0.347227	0.258666	0.517518	0.116474	0.457092	0.368253
t27	0.356903	0.471713	-0.00565536	0.26387	0.114077	0.274211	0.0486259	0.153816	0.055569
t28	0.06571	0.224223	0.383635	0.212825	0.239221	0.127791	-0.050636	0.245488	0.185747
t29	0.170301	0.237665	-0.0501201	0.12081	0.246531	0.210753	0.403732	0.228185	0.0740563
t30	0.0471498	0.141503	0.0404905	0.280162	0.120483	0.273985	-0.0016708	0.476946	0.367712
t31	0.357222	0.396713	-0.0189788	0.236001	0.0738938	0.223157	0.328149	0.159071	0.104069
t32	0.0909085	0.154976	0.309699	0.230733	0.0724423	0.248613	-0.0150098	0.404016	0.371145
avg	**0.1277**	**0.2932**	**0.2195**	**0.3633**	**0.3332**	**0.3647**	**0.2185**	**0.3014**	**0.1286**

Figure D.5: Fish-school array at 6 m s^{-1}

	8	8	8	8	8	8	8	8	8
	90	112.5	135	157.5	180	202.5	225	247.5	270
t01	0.367092	0.371082	0.4024	0.419186	0.409753	0.430035	0.438033	0.241305	0.158726
t02	0.168795	0.23198	0.441609	0.432837	0.413075	0.421231	0.402394	0.367645	0.362789
t03	0.364817	0.368665	0.410723	0.40572	0.402379	0.452276	0.19872	0.278084	0.102816
t04	0.150717	0.284307	0.463692	0.436444	0.423889	0.286965	0.263228	0.424673	0.196366
t05	0.205641	0.424369	0.274737	0.275554	0.423779	0.436789	0.460261	0.297931	0.144491
t06	0.111103	0.268848	0.202571	0.456791	0.407997	0.409685	0.41143	0.363997	0.362056
t07	0.364609	0.376889	0.409882	0.399052	0.406058	0.448542	0.0923922	0.116633	0.0575981
t08	0.142627	0.309226	0.464591	0.409592	0.417612	0.234141	0.306287	0.224819	0.123388
t09	0.148952	0.446366	0.227983	0.36959	0.26732	0.477357	0.249744	0.341315	0.0736597
t10	0.077365	0.330805	0.257019	0.480311	0.273504	0.381936	0.228132	0.445912	0.144931
t11	0.126705	0.232095	0.32035	0.226012	0.41943	0.409973	0.462474	0.325549	0.139756
t12	0.0611036	0.112589	0.0994676	0.455147	0.413379	0.401723	0.413719	0.37801	0.363377
t13	0.358189	0.391417	0.399645	0.395051	0.419591	0.469216	0.0766646	0.116157	0.0279726
t14	0.134936	0.337079	0.457815	0.40924	0.424796	0.179649	0.322196	0.190229	0.0872624
t15	0.137713	0.454169	0.237249	0.43168	0.307031	0.381362	0.0874641	0.270768	0.0635784
t16	0.0709039	0.388885	0.254289	0.480886	0.284817	0.326758	0.132992	0.225576	0.129106
t17	0.128484	0.218676	0.138349	0.31396	0.290157	0.480227	0.254559	0.401984	0.070694
t18	0.0638588	0.255455	0.0901792	0.388373	0.317788	0.436598	0.243923	0.454651	0.138542
t19	0.0865992	0.19283	0.336409	0.178445	0.428612	0.411431	0.455895	0.349457	0.135881
t20	0.0281769	0.110334	0.0829665	0.472522	0.428152	0.400289	0.403436	0.39326	0.359441
t21	0.361448	0.410164	0.223461	0.4312	0.304946	0.317607	0.0204589	0.210406	0.0603984
t22	0.143389	0.384615	0.316823	0.42534	0.381407	0.200655	0.0910897	0.267911	0.129326
t23	0.146231	0.416516	0.0984618	0.314229	0.208204	0.348928	0.146805	0.444456	0.0773793
t24	0.074043	0.42989	0.142492	0.351489	0.210183	0.318623	0.0995359	0.425506	0.152179
t25	0.124578	0.264553	0.097978	0.195294	0.390378	0.417547	0.326387	0.39644	0.14797
t26	0.0574048	0.202345	0.0209336	0.324914	0.308953	0.437862	0.226222	0.415832	0.365285
t27	0.35941	0.433626	0.0708869	0.298286	0.184569	0.316386	0.104675	0.20298	0.113879
t28	0.151757	0.333005	0.341436	0.259014	0.259344	0.204438	0.0182434	0.25491	0.20932
t29	0.198024	0.251953	0.0187506	0.199522	0.2653	0.256462	0.354286	0.333822	0.159486
t30	0.105735	0.193988	0.0984594	0.318558	0.189514	0.305179	0.073352	0.435812	0.364864
t31	0.359676	0.418526	0.0531074	0.259935	0.132795	0.295455	0.345569	0.287903	0.18125
t32	0.169914	0.288854	0.333464	0.301719	0.131811	0.268726	0.0566985	0.423399	0.366784
avg	**0.1734**	**0.3167**	**0.2434**	**0.3599**	**0.3296**	**0.3614**	**0.2427**	**0.3221**	**0.1741**

Figure D.6: Fish-school array at 8 m s^{-1}

	10	10	10	10	10	10	10	10	10
	90	112.5	135	157.5	180	202.5	225	247.5	270
t01	0.311561	0.312536	0.325351	0.327341	0.325391	0.329557	0.32932	0.265797	0.185266
t02	0.191224	0.258467	0.320763	0.321543	0.316366	0.320678	0.318417	0.306854	0.30379
t03	0.310966	0.314759	0.327425	0.320501	0.32171	0.332514	0.237714	0.292681	0.118525
t04	0.183008	0.285878	0.323657	0.327521	0.321262	0.27154	0.244734	0.3128	0.193567
t05	0.200637	0.322478	0.251068	0.26873	0.33152	0.33707	0.334114	0.294848	0.179663
t06	0.124991	0.284525	0.239333	0.3195	0.313521	0.314651	0.320124	0.305589	0.303434
t07	0.310922	0.312248	0.325337	0.324263	0.321817	0.332137	0.117971	0.151819	0.082964
t08	0.180141	0.293085	0.32155	0.315402	0.320792	0.254058	0.245647	0.195274	0.136644
t09	0.156884	0.332355	0.236661	0.292561	0.251765	0.334662	0.257405	0.316537	0.092307
t10	0.0953005	0.30638	0.261217	0.317004	0.25464	0.289789	0.237398	0.321386	0.153346
t11	0.139447	0.198691	0.254824	0.248276	0.331186	0.32568	0.332622	0.30263	0.179296
t12	0.0858257	0.145962	0.122331	0.319914	0.314087	0.318749	0.318943	0.306484	0.30332
t13	0.307695	0.316517	0.320476	0.31976	0.323241	0.33434	0.0933131	0.171815	0.056533
t14	0.176185	0.302513	0.321649	0.319283	0.322474	0.220231	0.263728	0.198439	0.104152
t15	0.142071	0.336059	0.241498	0.313766	0.272542	0.309492	0.147306	0.279267	0.0856705
t16	0.0870638	0.317473	0.258161	0.321575	0.26191	0.273896	0.155446	0.225669	0.134347
t17	0.1339	0.221213	0.158446	0.276693	0.265764	0.339473	0.257603	0.329189	0.0872289
t18	0.0856754	0.267669	0.150592	0.307725	0.274928	0.301968	0.245445	0.324752	0.142812
t19	0.103724	0.198581	0.272881	0.217165	0.332744	0.328446	0.332507	0.311378	0.178245
t20	0.0566437	0.164549	0.0981703	0.323538	0.315073	0.314532	0.314249	0.310557	0.300606
t21	0.306908	0.320786	0.245023	0.320171	0.29585	0.26615	0.0638262	0.241047	0.0873365
t22	0.184452	0.309766	0.274212	0.309634	0.306872	0.22579	0.114143	0.263552	0.141155
t23	0.154422	0.300986	0.153904	0.286752	0.20909	0.309202	0.17062	0.335855	0.0985109
t24	0.0951888	0.323764	0.168645	0.306056	0.211167	0.282938	0.156398	0.296305	0.159439
t25	0.137423	0.262553	0.118888	0.221445	0.314186	0.321698	0.279441	0.318777	0.18941
t26	0.0845878	0.235409	0.0650393	0.267967	0.29235	0.307992	0.247122	0.311599	0.299917
t27	0.305622	0.327082	0.126854	0.270197	0.215486	0.302687	0.128239	0.211995	0.133727
t28	0.19092	0.297903	0.271367	0.260833	0.234233	0.223603	0.0677659	0.255748	0.201227
t29	0.192982	0.256427	0.0679421	0.221552	0.238728	0.258978	0.27957	0.305753	0.197848
t30	0.126583	0.206672	0.123966	0.300169	0.218909	0.27145	0.127249	0.318912	0.299065
t31	0.30515	0.326869	0.080517	0.233081	0.156212	0.290984	0.287286	0.288199	0.211577
t32	0.202789	0.283276	0.279224	0.290673	0.156294	0.237007	0.0830913	0.318777	0.299222
avg	**0.1772**	**0.2795**	**0.2221**	**0.2935**	**0.2794**	**0.2963**	**0.2221**	**0.2809**	**0.1763**

Figure D.7: Fish-school array at 10 m s^{-1}

	12	12	12	12	12	12	12	12	12
	90	112.5	135	157.5	180	202.5	225	247.5	270
t01	0.185469	0.185263	0.183807	0.179415	0.183027	0.177839	0.178591	0.207499	0.181312
t02	0.179914	0.194144	0.156453	0.155612	0.161648	0.157908	0.162756	0.169887	0.172294
t03	0.186619	0.18794	0.182207	0.178942	0.182734	0.178286	0.18605	0.207542	0.124332
t04	0.183445	0.187479	0.153967	0.15751	0.16259	0.147623	0.202367	0.159135	0.182097
t05	0.18772	0.177028	0.209534	0.163301	0.183493	0.178649	0.176686	0.20388	0.185657
t06	0.128811	0.191174	0.173489	0.157183	0.161909	0.156948	0.160839	0.16926	0.172031
t07	0.18834	0.184179	0.182031	0.182666	0.182118	0.181532	0.151408	0.184737	0.0938654
t08	0.185915	0.1847	0.153221	0.163426	0.16356	0.150651	0.193115	0.181386	0.132665
t09	0.157932	0.177905	0.193783	0.157568	0.188308	0.175896	0.182016	0.198973	0.102358
t10	0.104846	0.180337	0.169046	0.154849	0.176403	0.136897	0.185943	0.157603	0.154601
t11	0.135179	0.184502	0.199005	0.164383	0.183283	0.183914	0.175623	0.201372	0.189069
t12	0.0961474	0.178431	0.152102	0.160452	0.161465	0.162182	0.160197	0.164091	0.172158
t13	0.189378	0.183751	0.179341	0.177782	0.181	0.172372	0.097356	0.199219	0.069351
t14	0.186706	0.180794	0.155971	0.164939	0.163189	0.164145	0.194124	0.181421	0.104033
t15	0.141724	0.177637	0.182097	0.162745	0.174984	0.196152	0.16895	0.210727	0.0912364
t16	0.0948236	0.171959	0.183507	0.152885	0.197293	0.144991	0.16654	0.168792	0.125624
t17	0.125619	0.177999	0.168237	0.163789	0.207247	0.172541	0.194231	0.191149	0.0952424
t18	0.0911369	0.197941	0.168055	0.177801	0.157539	0.141998	0.171599	0.155989	0.141935
t19	0.103873	0.186168	0.19983	0.173778	0.18137	0.182899	0.177383	0.197335	0.190898
t20	0.0693492	0.19125	0.100389	0.150257	0.160773	0.157654	0.158278	0.163652	0.172313
t21	0.188246	0.181409	0.180962	0.174087	0.17662	0.199709	0.112478	0.200275	0.0997453
t22	0.192158	0.170242	0.200771	0.154223	0.20177	0.16479	0.130023	0.167147	0.133997
t23	0.151247	0.169313	0.168121	0.181817	0.185275	0.18487	0.177127	0.188697	0.111169
t24	0.107548	0.172169	0.176058	0.165397	0.181358	0.16381	0.167215	0.148996	0.153935
t25	0.131657	0.180376	0.132852	0.178179	0.214016	0.174218	0.209129	0.18605	0.197658
t26	0.0971674	0.189508	0.114167	0.189875	0.156078	0.153573	0.16809	0.160792	0.170003
t27	0.187504	0.177511	0.167021	0.198258	0.182521	0.200387	0.142349	0.195308	0.144162
t28	0.196431	0.171125	0.201737	0.158702	0.196711	0.176898	0.118322	0.178864	0.159473
t29	0.160635	0.193858	0.117814	0.185909	0.202264	0.172537	0.207524	0.188481	0.202354
t30	0.137659	0.186562	0.14	0.181993	0.172713	0.183685	0.165596	0.15641	0.168529
t31	0.186771	0.179574	0.101806	0.18117	0.164181	0.174174	0.206854	0.178157	0.206374
t32	0.200296	0.161352	0.201112	0.155397	0.163775	0.176094	0.102879	0.159046	0.16743
avg	**0.1519**	**0.1817**	**0.1671**	**0.1689**	**0.1785**	**0.1702**	**0.1672**	**0.1807**	**0.149**

Figure D.8: Fish-school array at 12 m s^{-1}

Appendix E

Numerical Schemes

The following numerical schemes are required in the OpenFOAM settings:

- *timeScheme*: first and second time derivatives

- *gradSchemes*: gradient

- *divSchemes*: divergence

- *laplacianSchemes*: Laplacian

- *interpolationSchemes*: cell to face interpolations of values.

- *snGradSchemes*: component of gradient normal to a cell face.

- *wallDist*: distance to wall calculation, where required.

E.1   Gradient Schemes

The *gradSchemes* sub-dictionary contains gradient terms. The default discretization scheme that is primarily used for gradient terms is

```
default        Gauss linear;
```

The Gauss entry specifies the standard finite volume discretization of Gaussian integration which requires the interpolation of values from cell centres to face centres. The interpolation scheme is then given by the linear entry, meaning linear interpolation or central differencing. In some cases, particular involving poorer quality meshes, the discretization of specific gradient terms is overridden to improve boundedness and stability. The terms that are overridden in those cases are the velocity gradient.

```
grad(U)        cellLimited Gauss linear 1;
```

They use the *cellLimited* scheme which limits the gradient such that when cell values are extrapolated to faces using the calculated gradient, the face values do not fall outside the bounds of values in surrounding cells. A limiting coefficient is specified after the underlying scheme for which 1 guarantees boundedness and 0 applies no limiting; 1 is invariably used.

E.2   Divergence Schemes

The *divSchemes* sub-dictionary contains divergence terms, i.e. terms of the form $\nabla\cdot$, excluding Laplacian terms (of the form $\nabla \cdot (\Gamma\nabla...)$). This includes both advection terms, e.g. $\nabla \cdot (\mathbf{U}\nabla)$, where velocity $\mathbf{U}$ provides the advective flux, and other terms, that are often diffusive in nature. The fact that terms that are fundamentally different reside in one sub-dictionary means that the default scheme in generally set to none in divSchemes. The non-advective terms then generally use the Gauss integration with linear interpolation, e.g.

```
div(U)        Gauss linear;
```

The treatment of advective terms is one of the major challenges in CFD numerics and so the options are more extensive. The keyword identifier for the advective terms are usually of the form *div(phi,...)*, where phi generally denotes the (volumetric) flux of velocity on the cell faces for constant-density flows and the mass flux for compressible flows, e.g. *div(phi,U)* for the advection of velocity, *div(phi,e)* for the advection of internal energy, *div(phi,k)* for turbulent kinetic energy, etc.

The schemes are all based on Gauss integration, using the flux phi and the advected field being interpolated to the cell faces by one of a selection of schemes, e.g. *linear*, *linearUpwind*, etc. There is a bounded variant of the discretisation, discussed later. Ignoring 'V'-schemes (with keywords ending "V"), and rarely-used schemes such as Gauss *cubic* and *vanLeerV*, the interpolation schemes are as follows.

- *linear*: second order, unbounded.

- *linearUpwind*: second order, upwind-biased, unbounded (but much less so than linear), that requires discretisation of the velocity gradient to be specified.

- *LUST*: blended 75% linear/ 25%linearUpwind scheme, that requires discretization of the velocity gradient to be specified.

- *limitedLinear: linear*: scheme that limits towards upwind in regions of rapidly changing gradient; requires a coefficient, where 1 is strongest limiting, tending towards linear as the coefficient tends to 0.

- *upwind*: first-order bounded, generally too inaccurate to be recommended.

E.3   Surface Normal Gradients

It is worth explaining the *snGradSchemes* sub-dictionary that contains surface normal gradient terms, before discussion of *laplacianSchemes*, because they are required to evaluate a Laplacian term using Gaussian integration. A surface normal gradient is evaluated at a cell face; it is the component, normal to the face, of the gradient of values at the centres of the 2 cells that the face connects. A search for the default scheme for *snGradSchemes* reveals the following entries.

```
default        corrected;
default        limited corrected 0.33;
default        limited corrected 0.5;
default        orthogonal;
default        uncorrected;
```

The basis of the gradient calculation at a face is to subtract the value at the cell centre on

one side of the face from the value in the centre on the other side and divide by the distance. The calculation is second-order accurate for the gradient normal to the face if the vector connecting the cell centres is orthogonal to the face, i.e. they are at right-angles. This is the orthogonal scheme.

Orthogonality requires a regular mesh, typically aligned with the Catersian co-ordinate system, which does not normally occur in meshes for real world, engineering geometries. Therefore, to maintain second-order accuracy, an explicit non-orthogonal correction can be added to the orthogonal component, known as the corrected scheme. The correction increases in size as the non-orthonality, the angle α between the cell-cell vector and face normal vector, increases.

As α tends towards 90 degrees, e.g. beyond 70 degrees, the explicit correction can be so large to cause a solution to go unstable. The solution can be stabilised by applying the limited scheme to the correction which requires a coefficient ψ, $0 \leq \psi \leq 1$ where

$$
\psi = \begin{cases} \text{0 corresponds uncorrected} \\ \text{0.33 non orthogonal correction less than 0.5 times orthogonal part} \\ \text{0.5 non orthogonal correction less than the orthogonal part} \\ \text{1 corresponds to corrected} \end{cases}
$$

Typically, ψ is chosen to be 0.33 or 0.5, where 0.33 offers greater stability and 0.5 greater accuracy. The corrected scheme applies under-relaxation in which the implicit orthogonal calculation is increased by $\arccos \alpha$, with an equivalent boost within the non-orthogonal correction. The uncorrected scheme is equivalent to the corrected scheme, without the non-orthogonal correction, so includes is like orthogonal but with the $\arccos \alpha$ under-relaxation. Generally the uncorrected and orthogonal schemes are only recommended for meshes with very low non-orthogonality (e.g. maximum 5 degrees). The corrected scheme is generally recommended, but for maximum non-orthogonality above 70 degrees, limited may be required. At non-orthogonality above 80 degrees, convergence is generally hard to achieve.

E.4 Laplacian Schemes

The *laplacianSchemes* sub-dictionary contains Laplacian terms. A typical Laplacian term is $\nabla \cdot (\nu \nabla)$, the diffusion term in the momentum equations, which corresponds to the keyword `laplacian(nu,U)` in *laplacianSchemes*. The Gauss scheme is the only choice of discretization and requires a selection of both an interpolation scheme for the diffusion coefficient, i.e. ν in our example, and a surface normal gradient scheme, i.e. $\nabla \mathbf{U}$. To summarize, the entries required are:

```
Gauss <interpolationScheme> <snGradScheme>
```

The following entries are available.

```
default      corrected;
default      limited corrected 0.33;
default      limited corrected 0.5;
default      orthogonal;
default      uncorrected;
```

Bibliography

[1] S. Shamsoddin and F. Porté-Agel, "A large-eddy simulation study of vertical axis wind turbine wakes in the atmospheric boundary layer," *Energies*, vol. 9, no. 5, 2016.

[2] D. Berg, "The sandia legacy vawt research program, scientific and technological challenges in offshore vawts," tech. rep., Sandia National Laboratories, 2016.

[3] Seatwirl, "The future of offshore wind." https://seatwirl.com.

[4] J. T. Hansen, M. Mahak, and I. Tzanakis, "Numerical modelling and optimization of vertical axis wind turbine pairs: A scale up approach," *Renewable Energy*, vol. 171, pp. 1371–1381, 2021.

[5] I. Paraschivoiu, *Wind turbine design with emphasis on Darrieus concept*. Presses Internationales Polytechnique, 2002.

[6] H. Madsen, *The actuator cylinder: a flow model for vertical-axis wind turbines*. PhD thesis, Aalborg University Centre, 1982.

[7] N. Jensen, "A note on wind turbine interaction," Tech. Rep. Technical Report Ris-M-2411, Roskilde National Laboratory, Roskilde, Denmark, 1983.

[8] M. Abkar, "Theoretical modeling of vertical-axis wind turbine wakes," *Energies*, vol. 12, no. 1, 2019.

[9] R. W. Whittlesey, S. Liska, and J. O. Dabiri, "Fish schooling as a basis for vertical axis wind turbine farm design," *Bioinspiration & Biomimetics*, vol. 5, no. 3, p. 035005, 2010.

[10] D. Araya, A. Craig, M. Kinzel, and J. Dabiri, "Low-order modeling of wind farm aerodynamics using leaky Rankine bodies," *Journal of Renewable and Sustainable energy*, vol. 6, 2014.

[11] E. Svenning, "Implementation of an actuator disk in openfoam," tech. rep., Chalmers University of Technology, october 2010.

[12] P. Bachant, P. Goude, and M. Wosnik, "Actuator line modeling of vertical-axis turbines," *Physics - Fluid Dynamics*, 04 2018.

[13] M. Abkar, "Impact of subgrid-scale modeling in actuator-line based large-eddy simulation of vertical-axis wind turbine wakes," *Atmosphere*, vol. 9, no. 7, 2018.

[14] V. Mendoza and A. Goude, "Wake flow simulation of a vertical-axis wind turbine under the influence of wind shear," *IOP Conf. Series: Journal of Physics*, vol. 854, 2017.

[15] S. Hezaveh, E. Bou-Zeid, J. Dabiri, M. Kinzel, G. Cortina, and L. Martinelli, "Increasing the power production of vertical-axis wind-turbine farms using synergistic clustering," *Boundary-Layer Meteorology*, vol. 9, no. 169, p. 275–296, 2018.

[16] S. Zanforlin and T. Nishino, "Fluid dynamics mechanisms of enhanced power generation by closely-spaced vertical axis wind turbines," *Renewable Energy*, vol. 99, pp. 1213–1226, 2016.

[17] J. Bremseth and K. Duraisamy, "Computational analysis of vertical axis wind turbine arrays," *Theor. Comput. Fluid Dyn*, pp. 387–401, 2016.

[18] S. Giorgetti, G. Pellegrini, and S. Zanforlin, "CFD investigation of the aerodynamics interferences between medium solidity darrieus vertical axis wind turbines," *Energy Procedia*, vol. 81, pp. 227–239, 2015.

[19] A. Li, "Double actuator cylinder model of a tandem vertical-axis wind turbine counter-rotating rotor concept operating in different wind conditions," Master's thesis, Technical University of Denmark, 2017.

[20] Z. Cheng, H. A. Madsen, Z. Gao, and T. Moan, "Aerodynamic modeling of floating vertical axis wind turbines using the actuator cylinder flow method," *Energy Procedia*, vol. 94, pp. 531–543, 2016.

[21] H. Madsen, T. Larsen, L. Vita, and U. Paulsen, "Implementation of the actuator cylinder flow model in the hawc2 code for aeroelastic simulations on vertical axis wind turbines," in *In 51st AIAA Aerospace Sciences Meeting including the New Horizons Forum and Aerospace Exposition*, no. 51, AIAA, 2013.

[22] Z. Cheng, *Integrated dynamic analysis of floating vertical axis wind turbines.* PhD thesis, NTNU Norwegian University of Science and Technology, march 2016.

[23] P. G. Migliore, W. P. Wolfe, and J. B. Fanucci, "Flow curvature effects on darrieus turbine blade aerodynamics," *J. Energy*, vol. 4, no. 2, 1980.

[24] M. Claessens, "The design and testing of airfoils for application in small vertical axis wind turbines," Master's thesis, TUDelft, 2006.

[25] D. Marten, J. Wendler, G. Pechlivanoglou, C. Nayeri, and C. Paschereit, "Qblade: An open source tool for design and simulation of horizontal and vertical axis wind turbines," *International Journal of Emerging Technology and Advanced Engineering (IJETAE)*, vol. 3, pp. 264–269, 2013.

[26] M. Drela, "Xfoil: An analysis and design system for low Reynolds number airfoils," *Low Reynolds Number Aerodynamics, Lecture Notes in Engineering*, 1989. vol 54, Springer, Berlin, Heidelberg.

[27] A. Ning, "Actuator cylinder theory for multiple vertical axis wind turbines," *Wind Energ. Sci.,*, vol. 1, p. 327–340, 2016.

[28] F. Moukalled, L. Mangani, and M. Darwish, *The finite volume method in computational fluid dynamics an advanced introduction with OpenFOAM and Matlab.* Springer, 1st ed., 2016.

[29] J. Bardina, P. Huang, and T. Coakley, "Turbulence modeling validation, testing, and development," tech. rep., 1997.

[30] D. Wilcox, *Turbulence Modeling for CFD*. Anaheim: DCW Industries, 2nd ed., 1998.

[31] H. Versteeg and W. Malalasekera, *An Introduction to Computational Fluid Dynamics*. Prentince Hall, 1995.

[32] G. Larsen and K. Hansen, "Database on wind characteristics, contents of database bank, revision i.," tech. rep., Riso National Laboratory, Roskilde, June 2004.

[33] E. Martinez-Ojeda, F. J. Solorio-Ordaz, and M. Sen, "Vertical-axis wind-turbine computations using a 2d hybrid wake actuator-cylinder model," *Wind Energ. Sci.*, vol. 6, p. 1061–1077, 2021.

[34] J. O. Dabiri, "Potential order-of-magnitude enhancement of wind farm power density via counter-rotating vertical-axis wind turbine arrays," *Journal of Renewable and Sustainable Energy*, vol. 3, p. 043104, 2011.